Journal of Materials Chemistry A

Key factors boosting the performance of planar ZnFe2O4 photoanodes for solar water oxidation

Journal:	*Journal of Materials Chemistry A*
Manuscript ID	TA-ART-09-2021-007499.R1
Article Type:	Paper
Date Submitted by the Author:	05-Nov-2021
Complete List of Authors:	Polo, Annalisa; Università degli Studi di Milano, Dipartimento di Chimica Boudoire, Florent; Ecole Polytechnique Federale de Lausanne, SB ISIC LIMNO Lhermitte, Charles; Ecole Polytechnique Federale de Lausanne Liu, Yongpeng; Ecole Polytechnique Federale de Lausanne, Institute of Chemical Sciences and Engineering Guijarro, Néstor; EPFL SB ISIC LIMNO, Dozzi, Maria Vittoria; Università degli Studi di Milano, Diipartimento di Chimica Fisica ed Elettrochimica Selli, Elena; Universita degli Studi di Milano, Dipartimento di Chimica Sivula, Kevin; Ecole Polytechnique Federale de Lausanne, ; Swiss Federal Institute of Technology, Institute of Physical Chemistry

Journal of Materials Chemistry A
Materials for energy and sustainability

Guidelines for Reviewers

Thank you very much for agreeing to review this manuscript for *Journal of Materials Chemistry A*.

Journal of Materials Chemistry A is a weekly journal in the materials field. The journal is interdisciplinary, publishing work of international significance on all aspects of materials chemistry related to applications in energy and sustainability. Articles cover the fabrication, properties and applications of materials.

Journal of Materials Chemistry A's Impact Factor is **11.301** (2019 Journal Citation Reports®)

The following manuscript has been submitted for consideration as a

FULL PAPER

For acceptance, a Full Paper must report primary research that demonstrates significant **novelty and advance**, either in the chemistry used to produce materials or in the properties/ applications of the materials produced. Work submitted that is outside of these criteria will not usually be considered for publication. The materials should also be related to the theme of energy and sustainability.

When preparing your report, please:

- Focus on the **originality**, **importance**, **impact** and **reproducibility** of the science.
- Refer to the **journal scope and expectations**.
- **State clearly** whether you think the article should be accepted or rejected and give detailed comments (with references) both to help the Editor to make a decision on the paper and the authors to improve it.
- **Inform the Editor** if there is a conflict of interest, a significant part of the work you cannot review with confidence or if parts of the work have previously been published.
- **Provide your report rapidly** or inform the Editor if you are unable to do so.

Best regards,

Professor Anders Hagfeldt
Editor-in-Chief
EPFL, Switzerland

Dr Michaela Mühlberg
Executive Editor
Royal Society of Chemistry

Contact us

Please visit our reviewer hub for further details of our processes, policies and reviewer responsibilities as well as guidance on how to review, or click the links below.

What to do when you review

Reviewer responsibilities

Process & policies

Key factors boosting the performance of planar $ZnFe_2O_4$ photoanodes for solar water oxidation

Annalisa Polo[a], Florent Boudoire[b], Charles R. Lhermitte[b], Yongpeng Liu[b], Néstor Guijarro[b], Maria Vittoria Dozzi[a], Elena Selli[a] and Kevin Sivula[b]

[a]*Dipartimento di Chimica, Università degli Studi di Milano, via Golgi 19, I-20133 Milano, Italy*

[b]*Laboratory for Molecular Engineering of Optoelectronic Nanomaterials, École Polytechnique Fédérale de Lausanne (EPFL), Station 6, 1015 Lausanne, Switzerland*

Abstract

The performance of $ZnFe_2O_4$ photoanodes largely depends on their nanostructure, crystallinity and n-type doping, though decoupling their impact on photoactivity remains a challenge. Herein, the combined effects of the synthesis temperature and a reductive annealing post-treatment on the photoelectrochemical performance of planar $ZnFe_2O_4$ photoanodes are investigated in relation to a comprehensive range of film thickness, enabled by an optimized sol-gel synthetic approach. By eliminating the effects of nanostructure, a synergistic effect is revealed between the material crystallinity, controlled by synthesis temperature, and the n-type doping triggered by the H_2-treatment, which is maximum for the thickest photoactive layers. Intensity modulated photocurrent spectroscopy measurements performed *in operando* evidence the crucial impact of the synthesis temperature and the reductive treatment in inducing an effective surface charge injection and improved bulk charge transport, respectively, to enhance the photoelectrochemical performance of planar $ZnFe_2O_4$ films.

1. Introduction

Capturing and storing sunlight, the most plentiful renewable energy source, as chemical fuels in order to mitigate its intermittent and unpredictable nature, remains a key challenge towards realizing a fossil fuel-free, sustainable energy society.[1–3] Hydrogen (H_2) is a leading candidate as a clean fuel since it can be produced from water by solar-driven electrolysis.[4,5] A promising route in

this regard is photoelectrochemical (PEC) water splitting where direct semiconductor–liquid junctions (SCLJ) are used to drive the oxidation and reduction of water into O_2 and H_2, on a photoanode and a photocathode, respectively.[6,7] In principle a PEC tandem cell, where two complementary photoelectrodes are stacked to maximize the light harvesting efficiency, is a powerful strategy to enable unassisted and high efficiency solar water splitting.[8–10] However, realizing both high solar-to-hydrogen conversion efficiencies and robust device performance with this configuration has been limited by the development of semi-transparent semiconductor photoelectrodes with suitable band gap energy, high PEC activity, and stable performance.[8,11–13]

Indeed, identifying semiconducting materials for photoanodes that are capable of oxidizing water into oxygen with high efficiency and long-term stability is the major performance bottleneck of these devices. Metal oxide-based photoanodes stand out as promising candidates towards this aim, since they possess key requirements, such as low-cost, earth abundance, easily scalable processability, long-lasting durability under operation conditions and sufficiently oxidizing valence band maxima.[11,14–17] Several binary and ternary transition metal oxides, such as TiO_2, WO_3, $BiVO_4$ and Fe_2O_3, have been extensively studied, but their relatively wide band gap and/or poor semiconducting properties limit their practical application.[18–20] Therefore, the search for new ternary and multinary oxides able to absorb a large fraction of the solar spectrum and efficiently drive the oxygen evolution reaction (OER) remains an urgent need.[18]

In this regard, the spinel ferrite phases formed by ternary oxide compounds of iron(III) and a divalent metal (MFe$_2$O$_4$), have recently gained increasing interest for their excellent thermal and chemical stability. Moreover, the possibility to tune their band gap energy (1.4–2.1 eV) by selecting the divalent M cation (M = Zn, Mg, Cu, Ca, etc.) allows for controlling light harvesting in the visible range.[21–24] Specifically, $ZnFe_2O_4$ (ZFO) with a band gap energy of 2.0 eV has become a model system of this class of materials, as it shares many advantages of the well-studied hematite (Fe_2O_3) in addition to a 200 mV more negative photocurrent onset potential, which potentially allows for improved operation of a tandem cell.[19,25] However, the performance of ZFO photoanodes[25–34] remains far below

that of benchmark set by Fe_2O_3.[35,36] Detailed investigations revealed that a strong bulk recombination associated with a poor electron conductivity is a main issue with ZFO.[23,33,37,38] This limitation may be related to the extremely high temperature required to crystallize this class of materials.[26,27,39]

A post-synthesis thermal treatment under mild reductive conditions (*e.g.* under H_2 gas at 200 °C) is known to improve the conductivity of ZFO photoelectrodes through the introduction of oxygen vacancies acting as n-type dopants, thus increasing the majority carrier density of the material.[23,27,28,38,40,41] The reductive treatment of nanostructured ZFO films with a nanorod (NR) morphology led to a benchmark photocurrent density for solar water oxidation, and also pointed out that cation-site disorder may enhance the majority carrier transport in these electrodes even more than the film crystallinity, resulting in a superior separation of photogenerated charges.[40] However, although nanostructured architectures such as the NR morphology present many advantages for increasing charge collection efficiency (*e.g.* the channelized electron transport and reduced distance for minority charge carriers to reach the semiconductor/electrolyte interface), a detrimental light scattering side-effect compromises their use as top-layer photoanodes in PEC tandem devices.[11] Moreover, the NR morphology complicates decoupling and understanding the effects of the crystallinity and doping on the intrinsic material performance.

Accordingly, the development and optimization of ZFO films with a compact and planar geometry that simplifies the interpretation of the performance, and, due to their translucency, could also be more suitable in tandem cells is a recent research goal.[11,41] However, previous studies were limited by small film thickness (under 100 nm) due to the synthetic method employed. For this reason, in the present work we employ a modified sol-gel synthesis starting from a high precursor concentration to prepare planar ZFO films with different thickness, up to *ca.* 300 nm, in one single spin-coating deposition step. The PEC performance of these electrodes together with *in operando* intensity modulated photocurrent spectroscopy (IMPS) provide critical insight into the influence of the reductive hydrogen treatment on the fate of the photogenerated charges as a function of both the

film preparation temperature and the film thickness in the absence of morphological factors stemming from a nanostructured architecture.

2. Experimental Section

2.1 Chemicals and materials

The following chemicals were employed: $Zn(NO_3)_2 \cdot 6H_2O$ (ABCR), $Fe(NO_3)_3 \cdot 9H_2O$ (Acros Organics), NaOH (Reactolab SA) and Na_2SO_3 (Sigma-Aldrich). F-doped tin oxide (FTO) coated aluminoborosilicate glass (Solaronix) was used as conducting substrate.

2.2 Photoelectrode preparation

Thin $ZnFe_2O_4$ films with different thickness were prepared through the single-step spin-coating deposition of aqueous solutions containing different precursor concentrations, followed by a two-step heating procedure. The employed concentrations of the two metal nitrate precursors were determined in preliminary solubility tests, aiming at maximizing them while employing a suitable stoichiometry to obtain the desired phase. In this way, up to 40-fold higher nominal precursor concentrations were obtained with respect to those previously employed (*i.e.*, 0.25 M in Fe and 0.125 M in Zn).[11] All solutions were prepared with Millipore water (18.2 MΩ).

Prior to deposition, the FTO coated glass was thoroughly cleaned by sonication cycles in a soap/water mixture, acetone, ethanol, and finally in distilled water (15 min each) before plasma cleaning for 15 min. A static spin coating technique was used to deposit the precursor solution (150 μL) on the cleaned substrates, which were then spun at 500 rpm for 45 s. After spin coating, the films were first dried at 400 °C in air for 1 h, and then annealed in a tubular furnace preheated at 600 °C or 800 °C (for 20 min), followed by natural cooling to room temperature after switching the furnace off. Finally, the electrodes underwent a post-synthesis reductive treatment at 200 °C under a H_2 atmosphere for 1 h or 4 h. Powder samples for X-ray diffraction (XRD) analysis and Rietveld refinements (see next section) were prepared by annealing the precursor solutions at different temperature (600 °C, 700 °C and 800 °C) for 2 h.

2.3 Structural, morphological and optical characterizations

XRD data were collected using a Panalytical Empyrean system (Bragg-Brentano, 240 mm) equipped with a PIXcel-1D detector, a hybrid monochromator, and parallel beam optics. Raman spectra were recorded with a confocal Raman spectrometer (HORIBA Jobin Yvon XploRA PLUS) using a 532 nm wavelength laser for excitation. Powder X-ray diffraction (PXRD) analysis on the powder samples was conducted in a Bruker D8 Discover diffractometer using a non-monochromatized Cu-source, a Nickel filter and a LYNXEYE-XE energy-dispersive detector, which was set to filter Fe-fluorescence. Presented results were extracted from Rietveld refinements. Scanning electron microscope (SEM) data were collected using a Zeiss Gemini 300 scanning electron microscope in High Vacuum (HV) mode.

Transmittance and reflectance data were collected using a UV-3600 (Shimadzu) spectrometer equipped with an integrating sphere. The thickness of all synthesized films (reported in **Table 1**) was estimated using UV-Vis absorption and the estimated absorption coefficient α at the corresponding synthesis temperature. α values were calculated using the following equation:[42,43]

$$\alpha = -\frac{1}{h}\ln\left(\frac{T\%}{100 - R\%}\right) \#(1)$$

where h is the thickness (ca. 220-240 nm) of the reference sample for each synthesis temperature estimated from the cross-section SEM images (**Figure 1d**), *T%* and *R%* are the percent transmittance and reflectance values, respectively, of the same electrode at a selected wavelength. By comparing the linear regression plots, shown in **Figure S1**, of the absorbance at selected wavelengths *vs.* the estimated film thickness, $\lambda = 400$ nm was identified as the most suitable wavelength for α evaluation. The α values obtained according to **Eq. 1** for the two synthesis temperatures are $\alpha_{600}(400\text{ nm}) = 0.0085\text{ nm}^{-1}$ and $\alpha_{800}(400\text{ nm}) = 0.0093\text{ nm}^{-1}$.

2.4 Photoelectrochemical measurements

PEC measurements were carried out with a BioLogic SP-500 potentiostat connected to a cappuccino-type PEC cell (0.25 cm^2 active geometric area for the working electrode), in a three-

electrode configuration where a Ag/AgCl KCl (sat.) electrode and a Pt wire were used as reference and counter electrode, respectively. The light source was a 1000 W Xe arc lamp (Newport Oriel) calibrated using a Si photodiode to provide a photon flux corresponding to the AM 1.5 G spectrum (spectrally matched for $h\nu > 2.0$ eV). Intermittent-illumination linear sweep voltammetry (LSV) scans were acquired with a 20 mV s^{-1} scan rate by irradiating the electrode in both back (through the substrate-side) and front (through the electrolyte-side) configurations. The applied potentials acquired *vs.* Ag/AgCl in all measurements were converted to the reversible hydrogen electrode (RHE) using the equation: $E_{RHE} = E_{AgCl} + 0.059\ pH + 0.210$. LSV measurements were performed in either a 1.0 M NaOH aqueous electrolyte solution at pH 14, or in a 1.0 M NaOH solution containing also 0.5 M Na_2SO_3.

Photoelectrochemical impedance spectroscopy (PEIS) measurements were carried out in a 1.0 M NaOH electrolyte solution (pH 14) using a Bio-Logic SP-500 potentiostat coupled with the EC-Lab (V11.12) electrochemical platform. During each PEIS scan, the potential modulation frequency was scanned between 160 Hz and 50 mHz. A custom program written in the Python programming language was used to process and fit the PEIS data.

2.5 IMPS measurements and data analysis

IMPS tests were performed using a blue LED light generated by a customized light modulation system with 4 Cree XLamp MC-E LEDs. The sinusoidal modulation of the light intensity was controlled by a function generator (Tektronix AFG3021C), with a modulation depth of 10% and a frequency range from 80 kHz to 0.5 Hz. A three-electrode cappuccino-type cell was used, similar to that employed in the other PEC measurements. A Thompson Electrochem potentiostat (model 251) was used to control the applied potential on the working electrode and the photocurrent response was recorded by a digital oscilloscope (Tektronix DPO7254C) via a 50 Ω resistor (Velleman E6/E12) in series with a platinum counter electrode. IMPS data were processed and fitted using a custom program written in Igor Pro (WaveMetrics) and Origin Pro (OriginLab).

3. Results

To gain insight into the effect of the ZFO preparation temperature and the reductive hydrogen treatment on the photogenerated carrier transport and transfer, a series of planar ZFO electrodes was prepared using 8 different precursor concentrations, as reported in **Table 1**. The films obtained by spin coating the different precursor solutions were annealed at 600 °C or at 800 °C. Similar thickness values, determined by UV-vis absorption measurements (see Section 2.3), were obtained for the as-prepared ZFO films, independently of the synthesis temperature, as shown in **Table 1**.

Table 1. Adopted precursor solution concentrations and corresponding films thickness after heating at 600 or 800 °C.

$[Fe^{3+}]$ / M	**$[Zn^{2+}]$ / M**	**Thickness @ 600 °C / nm**	**Thickness @ 800 °C / nm**
0.5	0.25	60	50
1.0	0.5	70	70
1.5	0.75	80	90
2.0	1.0	100	100
2.5	1.25	140	120
5.0	2.5	160	160
7.5	3.75	220	240
10	5.0	240	310

Annealed films were directly employed in PEC measurements (coded as “pristine” samples) or underwent a further hydrogen treatment for 1 h or 4 h at 200 °C, to increase their carrier conductivity. All investigated ZFO electrodes are labelled as ZFO_X@Y, with X indicating the film thickness in nm, Y the annealing temperature in Celsius.

3.1 Structural, morphological and optical characterization

The phase composition and crystal structure of the as-prepared ZFO films were evaluated using XRD and Raman spectroscopy. Results obtained for the 160 nm-thick films annealed at 600 °C or 800 °C, are reported in **Figure 1**. The XRD patterns in **Figure 1a** only display the reflections

typical of cubic spinel $ZnFe_2O_4$ (JCPDS: 01-089-1010) and the diffraction peaks of SnO_2 associated to the FTO substrate (marked by asterisks). No signals for other segregated phases can be discerned. The peaks at about 2θ = 30°, 35.2°, 43°, 53° and 56.6° are indicative of the (220), (311), (400), (422) and (511) crystal planes, respectively, of the pure $ZnFe_2O_4$ phase, which crystallizes with a *Fd3m* space group.[23,26,38] The intensity of these reflections increases when the annealing temperature passes from 600 °C to 800 °C, which is an indication of the enhanced crystallinity of the films, in line with previous results on ZFO NR films.[40] Also, as established for ZFO NR films, the mild post-synthesis hydrogen treatment does not change the crystal structure.[23,26,27]

The Raman spectra over a wide range (100-1800 cm^{-1}) reported in **Figure 1b** further confirm the crystal phase and the absence of parasitic phases in the thin films prepared at 600 °C or 800 °C. In both cases, the weak feature appearing at 245 cm^{-1} and the three bands centred at 352, 506 and 629 cm^{-1} can be identified as the E_g, F_{2g} (two modes) and A_{1g} first-order Raman active modes typical of ZFO.[44] Also the broad weak feature at around 1120 cm^{-1} can be assigned to ZFO,[45] despite its similarity with the Raman signature of magnetite (Fe_3O_4).[46,47] More importantly, the absence of the characteristic intense signal of α-Fe_2O_3 at 1320 cm^{-1} and of the broad band above 1400 cm^{-1} typical of γ-Fe_2O_3 confirms the absence of undesired hematite[48,49] or maghemite,[50] respectively.

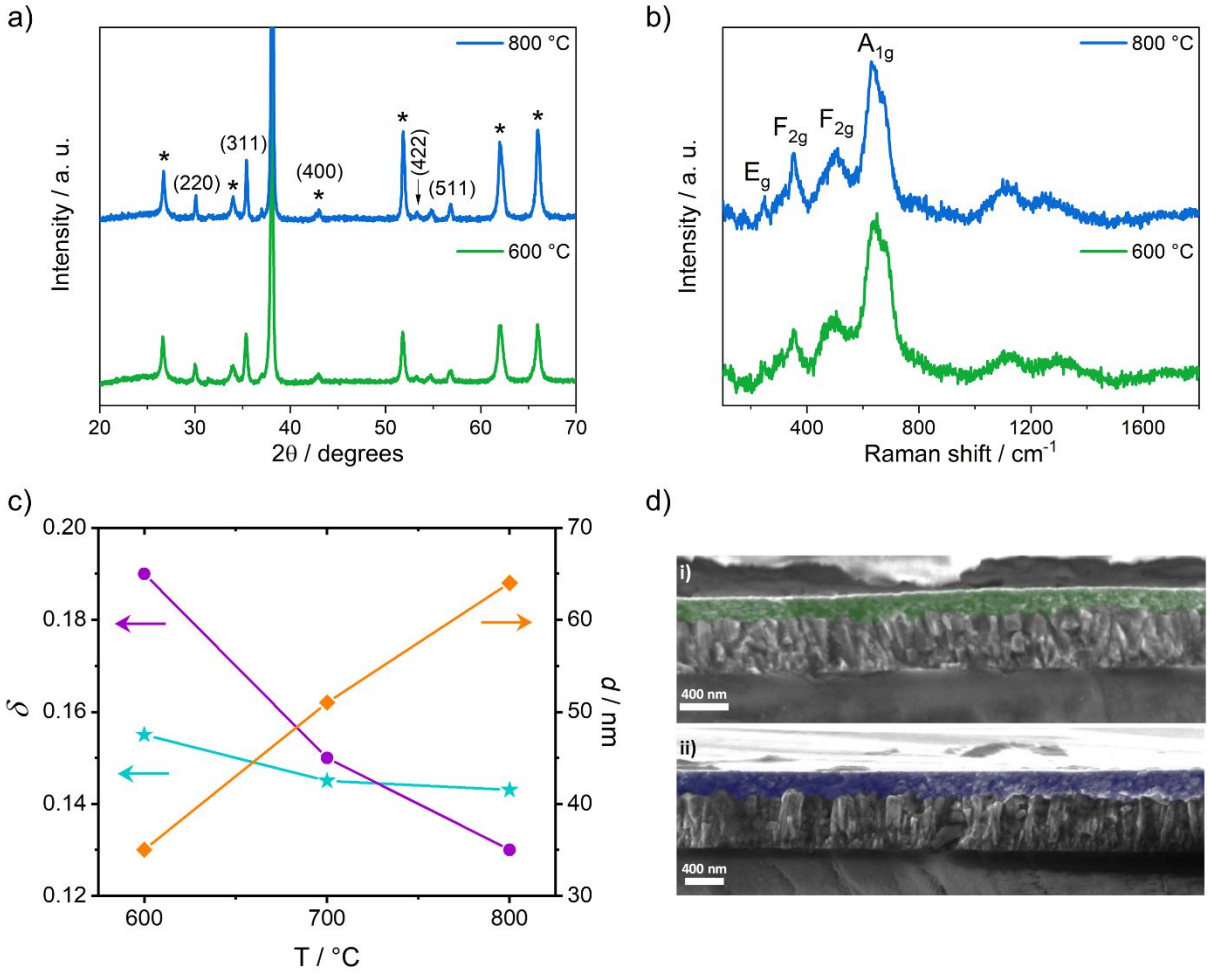

Figure 1. (a) XRD patterns and (b) Raman spectra of representative ZFO films annealed at 600 °C and 800 °C; (c) trends in the spinel inversion degree δ for our planar ZFO films (purple circles) and for ZFO NR electrodes (cyan stars, reproduced from ref. 38) and in the estimated crystalline domain size d (orange diamonds) *vs.* the synthesis temperature; (d) cross section SEM images of the (i) *ca.* 220 nm and (ii) *ca.* 240 nm-thick films annealed at 600 °C (Mag = 25.62 K X) and 800 °C (Mag = 20.55 K X), respectively, employed for the α evaluation reported in Section 2.3.

Despite the apparent phase purity of our ZFO thin films, additional investigation of the crystallinity of the material prepared via our sol-gel route is valuable considering the crystal structure of $ZnFe_2O_4$, which can exist in normal and inverted configurations. Indeed, typically ZFO possesses an almost normal spinel crystal structure composed of a cubic closed-packed array of oxygen atoms with the Zn^{2+} and Fe^{3+} ions located at the tetrahedral and octahedral sites, respectively.[51] However, cation inversion can occur and the degree of inversion (δ), defined as the fraction of tetrahedral sites occupied by Fe^{3+} ions, is known to mainly affect the magnetic behaviour of spinel ferrites.[52,53]

According to Thota *et al.*,[39] the A_{1g} mode in Raman spectra (**Figure 1b**), which is representative of the symmetric stretching of tetrahedral units, may split into two separate peaks associated with the lattice vibrations in the tetrahedral positions of both Zn and Fe cations, in the presence of an inversion degree. Based on this, the only slight A_{1g} mode split detectable in the peaks at 648 and 680 cm^{-1} of both Raman spectra shown in **Figure 1b** may indicate a partial inversion degree in the synthesized films.

Note that δ was suggested to influence the PEC properties of ZFO samples with NR morphology even more than their crystallinity degree.[40] Accordingly, we next estimated the crystalline domain size and cation inversion as a function of the synthesis temperature via the Rietveld refinement of PXRD patterns (**Figure S2**) of ZFO powders prepared at 600 °C, 700 °C and 800 °C using a procedure similar to that employed to prepare our thin films. In **Figure 1c** we display the values of δ, and the crystalline domain size (estimated by the integral breadth), d, as a function of the synthesis temperature. The same inverse behaviour for δ and d is observed with increasing preparation temperature as for ZFO NR samples,[40] although with a significantly different relative variation degree of these two parameters. In particular, while d monotonically increases by *ca.* 50% when rising the preparation temperature from 600 °C to 800 °C, the cation disorder δ exhibits only a minor decrease, from 0.15 to 0.14, for the same synthesis temperature increase. A much higher decrease in cation disorder was found for the ZFO NR electrodes within the same temperature range, with δ dropping from *ca.* 0.20 to 0.13 (data reproduced in Figure 1c for comparison).[40] Moreover, the maximum δ value of 0.15 achieved in the case of the planar ZFO films is far below $\delta = 1$ expected for a totally inverted spinel structure, suggesting that our as-prepared planar ZFO films primarily exhibit the normal spinel phase. The difference in the trend of δ between the planar films and the NR films is likely due to the synthesis method, where for the NR morphology an intermediate goethite phase of FeOOH is used. On the other hand, with respect to the crystal domain size, the remarkable increase (*ca.* 50%) of d from 35 to 65 nm (**Figure 1c**) in the planar films, which is comparable with the *ca.*

70% increase observed in NR films,[40] indicates a significant enhancement in crystallinity upon rising the synthesis temperature, in agreement with other reports.[45]

The morphology of the ZFO films was next examined by electron microscopy. **Figure 1d** shows representative cross-section SEM images of films prepared starting from the 7.5 M in [Fe^{3+}] and 3.75 M in [Zn^{2+}] ZFO precursor solution and prepared at either 600 °C (**Figure 1d i**) or 800 °C (**Figure 1d ii**). A planar film geometry is observed with dense and compact layers composed of interconnected nanoparticles with comparable thickness in the 220–240 nm range, regardless of the synthesis temperature.

3.2 Photoelectrochemical performance

Typical current density *vs.* applied potential (*J-V*) curves were collected under standard water oxidation conditions (intermittent 1-Sun illumination, 1.0 M NaOH electrolyte), to investigate how the different parameters (*i.e.* the synthesis temperature, film thickness, and hydrogen treatment) affect the PEC performance. **Figure 2** summarizes the *J-V* results in a plot of the photocurrent density at 1.5 V *vs.* RHE as a function of the film thickness, recorded under both back (substrate-side) and front (electrolyte-side) illumination of either the pristine or the hydrogen-treated electrodes prepared at 600 or 800 °C. The reported values are averaged over 5 electrodes prepared in the same conditions (see **Figure S3**). The relatively small error bars underline the reproducibility of the adopted synthesis method and post-synthesis hydrogen treatment. The results shown in **Figure 2** for hydrogen-treated electrodes refer to a 1 h-long exposure to H_2 flux, as prolonging the reductive treatment up to 4 h did not produce any further PEC performance improvement, as shown in **Figure S4**. This suggests that the film composition equilibrium in terms of oxygen vacancies was already reached after 1 h-long reductive treatment.

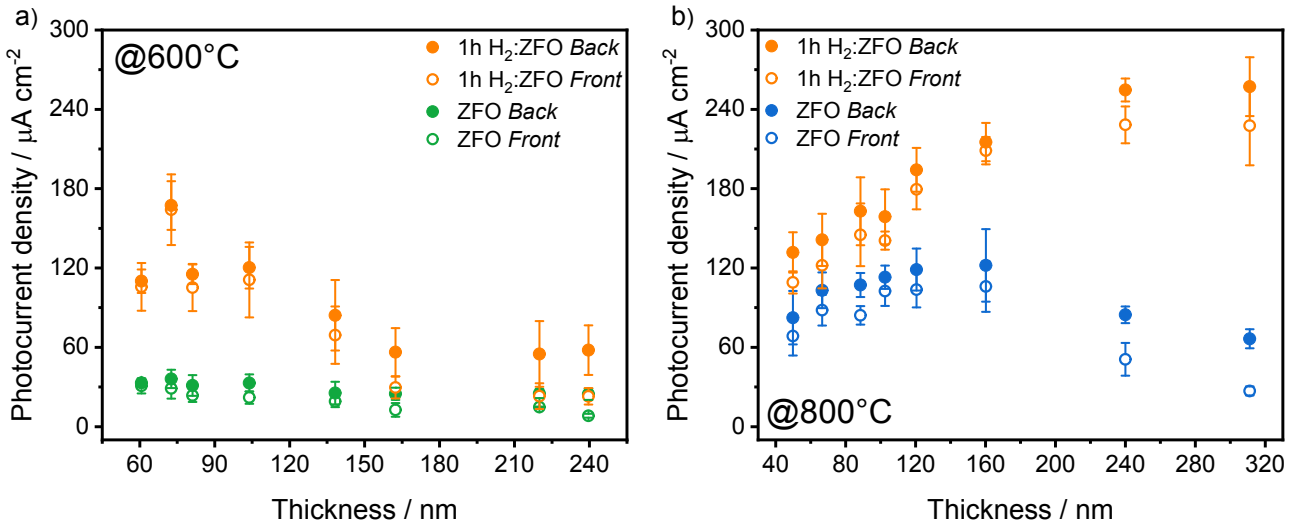

Figure 2. Photocurrent density (*J*) values as a function of the film thickness recorded with (a) the 600 °C and (b) the 800 °C electrodes at 1.5 V *vs.* RHE, before (pristine, green and blue) and after 1 h-long H_2-treatment (orange). Reported *J* values are the average of linear sweep voltammetry measurements with different samples in 1.0 M NaOH solution under either back (full circles) or front side (void circles) irradiation.

A clearly different behaviour for the pristine and the H_2 treated electrodes depending on the synthesis temperature is revealed by the data in **Figure 2**. Focusing on pristine films, the electrodes prepared at 600 °C (**Figure 2a**, green markers) exhibit a low photocurrent (below 40 μA cm^{-2}) that is insensitive to film thickness. In view of the relatively low crystallinity of the pristine 600 °C films, as evidenced by the *d* values reported in **Figure 1c**, the poor performance is consistent with a limitation in photogenerated charge transport. In contrast, the higher crystallinity of the films prepared at 800 °C, and likely the diffusion of Sn^{4+} dopant from the FTO substrate[23], correlated to a higher activity of the pristine electrodes, with a bell-shaped trend of the photocurrent *vs.* the film thickness and a maximum of 130 μA cm^{-2} around 160 nm, followed by a decrease for thicker films (**Figure 2b**, blue markers). This behaviour is also consistent with a limitation in photogenerated charge transport in films with thickness greater than 160 nm and the lower performance of the thicker films from the front side illumination points to a limitation in the transport of the majority charge carriers.

After H_2-treatment, the overall PEC performance increased but to a very different extent depending on the film thickness and preparation temperature. Indeed, while among the hydrogen-treated less crystalline (600 °C) electrodes the maximum photocurrent was recorded at a low thickness

(70 nm), followed by a drop with increasing thickness (**Figure 2a**, orange markers), the reduction treatment applied to more crystalline films (800 °C) induced a progressive enhancement in PEC performance with increasing film thickness, up to a plateau at 240 nm (**Figure 2b**, orange markers). The behaviour here observed for electrodes of thickness smaller than 100 nm is consistent with our previous results on ZFO planar films with similar thickness (under 100 nm),[41] while a much larger increase in performance after hydrogenation can be observed for the more crystalline (800 °C) electrodes series at the highest film thicknesses. For both preparation temperatures a maximum 4-fold enhancement in photocurrent was obtained upon H_2-treatment, though largely different absolute photocurrent values were attained in the two cases. In fact, the maximum photocurrent density of the hydrogen-treated electrodes initially prepared at 600 °C was only 160 μA cm^{-2}, while the combination of a higher (800 °C) preparation temperature and a subsequent hydrogen treatment boosted the photocurrent density of thicker photoactive layers up to 260 μA cm^{-2}, the maximum value attained in the present study.

To highlight the effects of H_2-treatment on films with different thickness prepared at the two temperatures, we focused on the results obtained with the 70 nm- and the 240 nm-thick films of each series. **Figure 3** shows the complete *J-V* curves recorded with these electrodes, either before or after H_2-treatment, under back side illumination. These curves exhibit typical n-type photoanode behaviour, with a photocurrent onset around 0.8 V *vs.* RHE, in agreement with previous studies,[11,23,39–41] and sharp transient photocurrent spikes at low bias, indicative of relatively high interfacial recombination, until a higher bias is attained where charges are extracted without accumulation and recombination. The transient spikes are more pronounced in the case of less crystalline films prepared at 600 °C. Moreover, the hydrogen treatment has a different impact on the shape of the *J-V* curve, depending on the thickness and preparation temperature. In fact, a higher saturation photocurrent (at high bias, *e.g.* 1.5 V *vs.* RHE) and an improved photocurrent onset in the low applied potential region were achieved upon H_2-treatment of optimal ZFO_70@600 (**Figure 3a)** and ZFO_240@800 (**Figure 3d**). In contrast, only a minor performance increase was attained upon

hydrogen treatment of ZFO_240@600 (**Figure 3b**), while treatment of ZFO_70@800 induced a performance decrease with a later photocurrent onset potential and a lower fill factor, compared to the pristine film (**Figure 3c**).

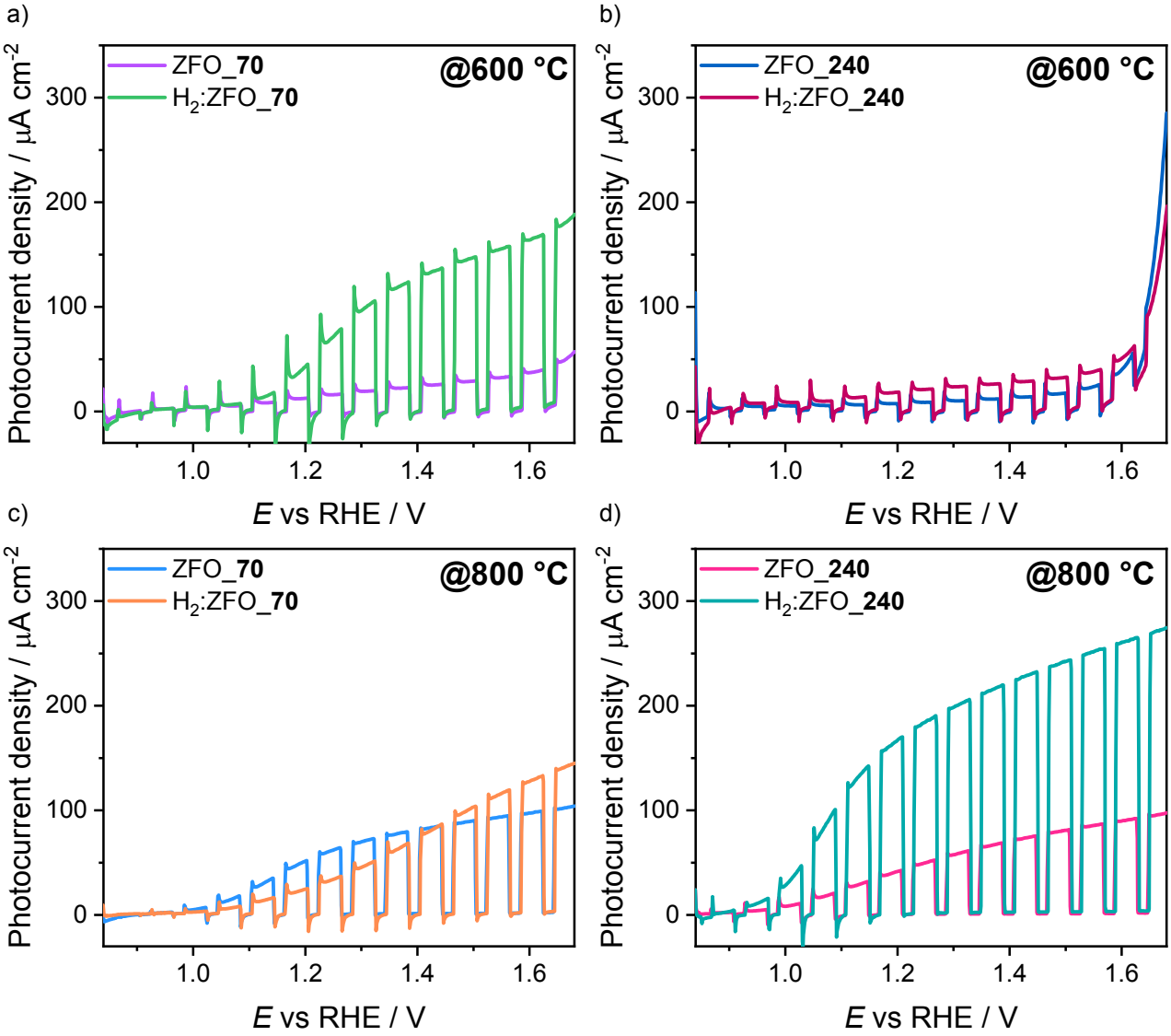

Figure 3. LSV plots recorded in 1.0 M NaOH electrolyte solution under back side irradiation, with 70 nm- and 240 nm-thick films prepared at (a,b) 600 °C or (c,d) 800 °C, before and after 1 h-long H_2 treatment.

The photocurrent onset potential of water oxidation is very sensitive to the presence of defects that cause surface recombination, due to the narrow width of the space charge layer in the low applied potential region.[54] Indeed, an increased surface defect concentration can cause Fermi-level pinning which may be reflected by a delay of the photocurrent onset potential with respect to the flatband potential.[23,45] Thus, the delayed photocurrent onset potential of the H_2-treated ZFO_70@800 electrode compared to the pristine one may indicate that the hydrogen treatment has a detrimental

effect on the surface properties of this sample, *e.g.* by introducing oxygen vacancies acting as surface trap states.[27,33,55]

To shed light onto the origin of the different impact of the H_2 treatment onto the PEC performance of ZFO films, depending on both their thickness and synthesis temperature, the bulk charge separation and the surface charge injection contributions to the overall photocurrent were decoupled by using sacrificial conditions[56] (Na_2SO_3 hole scavenger, see **Figure S5**) to extract the photogenerated charge separation efficiency (η_{sep}) and the minority charge carrier injection efficiency (η_{inj}). Indeed, the water oxidation photocurrent density can be expressed as $J_{H2O} = J_{abs}\,\eta_{sep}\,\eta_{inj}$, where J_{abs} is the theoretical maximum photocurrent density considering the light absorbed by each film, calculated from the integration of the product between the standard AM 1.5 G solar spectrum and the absorption spectrum of the electrode, over the proper absorption wavelengths range. Analogously, by assuming a 100% charge injection efficiency for Na_2SO_3 oxidation ($\eta_{inj} = 1$),[56] the photocurrent of sulfite oxidation (J_{Na2SO3}) is such that $J_{Na2SO3} = J_{abs}\,\eta_{sep}$, from which η_{sep} can be simply obtained by dividing the photocurrent measured in the presence of the Na_2SO_3 hole scavenger by J_{abs}. From the combination of the two photocurrent expressions (in the presence and absence of hole scavenger) one can finally calculate η_{inj}, which is equal to the ratio between J_{H2O} and J_{Na2SO3}.

The calculated efficiencies for the thinnest and thickest films of the two investigated electrode series are reported in **Figure 4** as a function of the applied potential. In all cases, η_{sep} values are much lower than η_{inj} values, indicating that the photocurrent response of our planar ZFO photoanodes is ultimately governed by a severe bulk recombination, possibly due to either a very low mobility and diffusion length of the carriers (*e.g.* due to polaron formation) or a high density of bulk defects. The bulk charge separation efficiency of the pristine samples typically increases gradually with increasing bias, due to the progressive widening of the depletion region adjacent to the electrode/electrolyte interface,[56] though it remains below 4% in all cases. These low η_{sep} values are in line with those reported for nanostructured ZFO[23,26–28,57] and decrease when moving from the thinner (**Figure 4a,c**) to the thicker films (**Figure 4b,d**) within each electrodes series, likely due to the increased probability

of bulk recombination with increasing thickness. A slight increase in charge separation can be observed when moving from samples annealed at 600 °C to those at 800 °C when considering the same thickness (Figure 4). This evidences the minor impact of the synthesis temperature on η_{sep}. Moreover, the H_2 treatment induces a conspicuous improvement of the charge separation efficiency compared to that of the pristine films, up to a maximum 3-fold enhancement at 1.5 V *vs.* RHE (**Figure 4c**); only for the poorly crystalline thicker film, exhibiting an intrinsically low η_{sep}, this remains low also after H_2-treatment (**Figure 4b**). This can be reasonably explained by the larger amount of charge carriers that should be produced by a thicker film and that, in case of poor crystallinity, may lead to an increased charge accumulation at the SCLJ,[23,26,27,33,55,58] which can be responsible for the lack of improvement in η_{sep} besides η_{inj} after H_2-treatment.

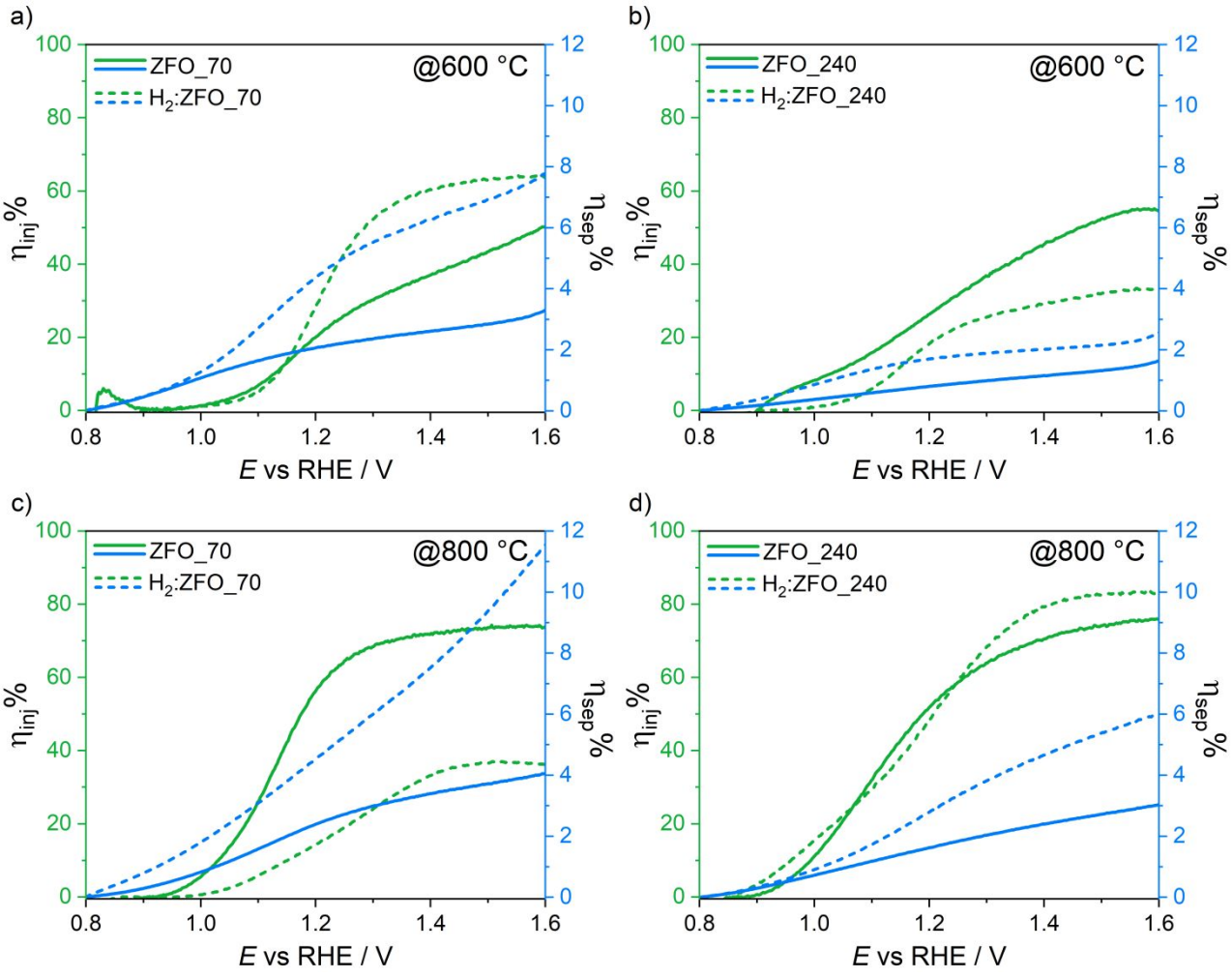

Figure 4. Charge injection (η_{inj}, green) and charge separation (η_{sep}, blue) efficiencies of the 70 nm- and 240 nm-thick films prepared at either (a,b) 600 °C or (c,d) 800 °C, before (continuous lines) and after 1 h-long H_2-treatment (dashed lines).

In contrast to its minor effects in the bulk charge separation efficiencies, the synthesis temperature has a great impact on the charge transfer efficiencies at the SCLJ interface. In fact, focusing on pristine samples, the more crystalline films prepared at 800 °C (**Figure 4c,d**) exhibit a η_{inj} close to 80% already at 1.4 V *vs.* RHE, which is double than that shown by the less crystalline electrodes annealed at 600 °C (**Figure 4a,b**). Moreover, for the electrodes annealed at 800 °C, this plateau value is achieved with a steeper η_{inj} increase at the photocurrent onset potential compared to the electrodes prepared at 600 °C, which indicates an efficient mitigation of surface recombination with increasing band bending.[23,56] A similar η_{inj} behaviour, independent of the film thickness, was observed with ZFO electrodes with NR morphology[26,40] annealed at similar temperatures.

On the other hand, the impact of the H_2 treatment on the surface injection strictly depends on both the film thickness and the preparation temperature, inducing a slight improvement for best performing ZFO_70@600 and ZFO_240@800 in the high potential region. This indicates that the hydrogen treatment has a little impact on the surface injection properties of planar ZFO samples.

3.3 Intensity Modulated Photocurrent Spectroscopy

PEC analyses conducted in the presence of sacrificial agents might not be representative of true water oxidation conditions since either the space charge properties (*e.g.* band-bending) or the charge accumulation at the photoanode surface can be influenced by the nature of the redox species involved in the electrochemical reaction at the film/electrolyte interface.[59] Therefore, caution should be taken in evaluating η_{sep} and η_{inj} for water oxidation, which is affected by a large surface kinetics bottleneck, from measurements carried out under sacrificial conditions, *i.e.* under the assumption that no charge accumulation occurs at the SCLJ. In fact, especially in the presence of a significant charge accumulation at the SCLJ under sluggish oxidation conditions, η_{sep} and η_{inj} values estimated from sacrificial measurements may considerably differ from the real ones. For this reason and aiming at validating the results obtained from PEC measurements in the presence of Na_2SO_3, η_{sep} and η_{inj} were also evaluated *in operando* by means of IMPS measurements, conducted under water photo-oxidation conditions in 1.0 M NaOH electrolyte. IMPS has indeed proved to be a powerful frequency domain

tool to unequivocally decouple the bulk and surface contributions of photoanodes by their respective time constants.[60,61]

The IMPS response for the same eight investigated electrodes shown in **Figure 4** is shown in **Figure 5** as Nyquist plots of the complex photocurrent at 1.5 V *vs.* RHE, which can be directly compared to the *J* at the same bias reported in **Figure 2**.

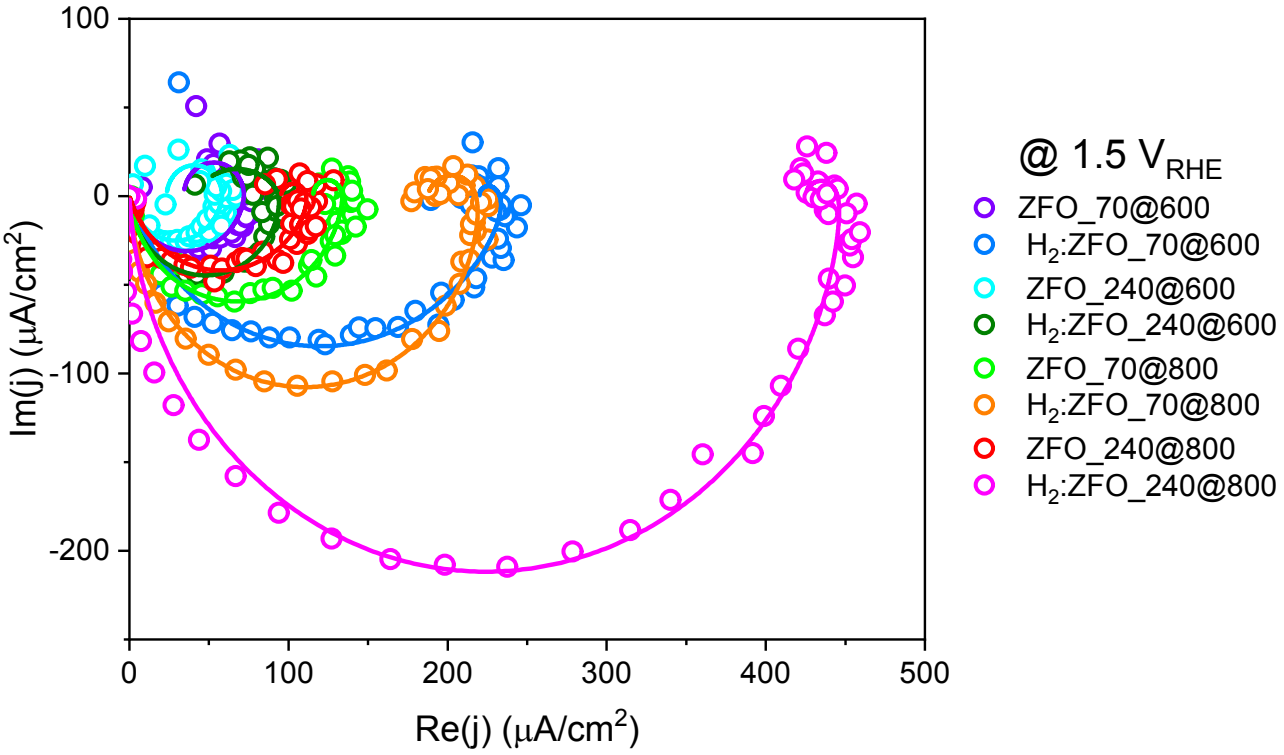

Figure 5. IMPS analyses at 1.5 V *vs.* RHE for the 70 nm- and 240 nm-thick films prepared at either 600 °C or 800 °C. The represented raw data (circles) and fitted model (lines) were obtained upon normalization to the electron current recorded at the IMPS setup.

All Nyquist plots are composed of two semicircles: the negative semicircle located in the lower quadrant and representative of the higher frequency process (shorter time constant), corresponding to charge transport in the bulk, and the positive semicircle located in the upper quadrant and associated with surface recombination occurring at lower frequencies (longer time constant).[62] Specifically, the amplitudes of the negative and positive semicircles are directly indicative of the flux of holes arriving to the SCLJ that are available for water oxidation (J_h) and the flux of holes that are lost by surface recombination (J_r), respectively. Therefore, the significantly smaller surface recombination semicircle in comparison with the bulk transport semicircle observable

in all reported cases (in **Figure 5**) indicates that a large steady state photocurrent is available for water oxidation at the surface of our planar ZFO photoanodes, in analogy with other metal oxide photoanodes.[63,64] All details about the IMPS model fitting and the extracted parameters, *i.e.* two photocurrent amplitudes (J_h and J_r) and the corresponding time constants for bulk hole current (τ_h) and surface recombination (τ_r), are reported in the Supporting Info, **Figure S6**. On the basis of model employed for the IMPS analysis,[62] an accurate estimate of the η_{sep} and η_{inj} parameters *in operando* can be pursued by simply calculating them as $\eta_{sep} = J_h/J_{abs}$ (where J_{abs} is the maximum photocurrent expected for each ZFO film based on its absorbance spectrum) and $\eta_{inj} = (J_h - J_r)/J_h$. **Figure 6** shows the comparison of these quantities extracted at 1.5 V *vs.* RHE for all investigated electrodes.

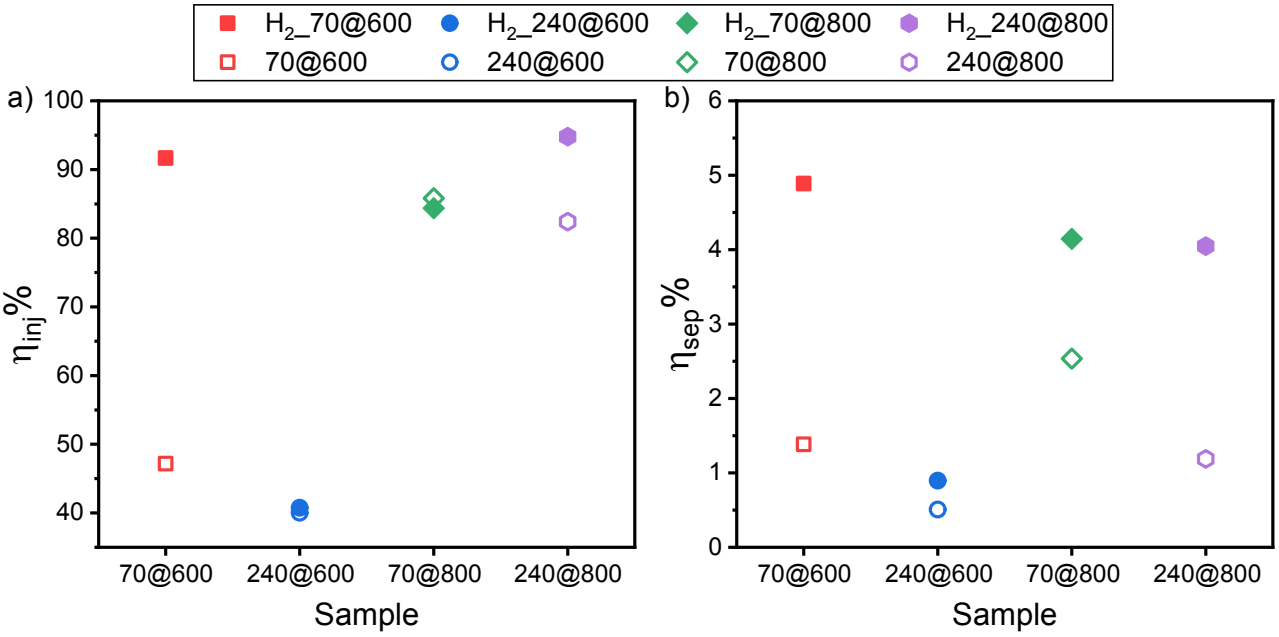

Figure 6. (a) Charge injection (η_{inj}) and (b) charge separation (η_{sep}) efficiencies calculated from IMPS data at 1.5 V *vs.* RHE, for the 70 nm- and 240 nm-thick films prepared at either 600 °C or 800 °C, before and after 1 h-long H_2-treatment.

The results of IMPS measurements conducted *in operando* confirm the trends of η_{sep} and η_{inj} obtained from PEC measurements in the presence of a sacrificial agent. The huge discrepancy between the surface injection and the bulk separation efficiencies is even more marked in this case, with maximum values of 95% (η_{inj}) and 5% (η_{sep}), respectively, and accounts for bulk charge separation as main performance limiting issue. The already-assessed effects of both synthesis

temperature and H_2 treatment on the two decoupled contributions, in relation to the film thickness, are confirmed. While the charge injection efficiency doubles from *ca.* 40% to *ca.* 80% in pristine samples prepared at higher temperature, regardless of the film thickness, H_2-treatment does not markedly influence the charge transfer efficiency at the photoanode surface, except for one case (**Figure 6a**). In fact, beyond the highest increase in η_{inj} detected for the hydrogen-treated thinner film prepared at 600 °C compared to its pristine form, a slight improvement of the surface injection properties occurs after H_2-treatment also for the thicker electrode prepared at 800 °C, likely induced by the passivation of surface states affecting the performance of the pristine samples.

On the other hand, the calculated charge separation efficiencies (**Figure 6b**) appear very sensitive to both the film thickness and the reductive treatment. In agreement with the results obtained under sacrificial conditions, the η_{sep} values of the pristine films decrease with increasing film thickness, for both synthesis temperatures. Consequently, the modest improvement in charge separation induced by the higher synthesis temperature can be appreciated only for the thinner film of the series.

In this picture, H_2 treatment plays a crucial role by inducing a remarkable improvement of the bulk charge separation in almost all cases, up to a maximum 4-fold enhancement observed with best performing ZFO_70@600 and ZFO_240@800. Moreover, as a result of the higher H_2-treatment efficiency observed with the thicker film within the 800 °C series, its η_{sep} attains the same value as the reduced form of the thinner film, despite the two electrodes exhibit significantly different efficiencies prior to H_2-treatment. A different extent of η_{sep} increase upon H_2-treatment can be observed within the 800 °C electrodes series, with the highest η_{sep} relative increase attained with the thickest ZFO_240@800 electrode. This can be explained by considering the different strength of the electric field resulting from polarizing the two samples (especially at a potential as high as 1.5 V *vs.* RHE), depending on their thickness and doping density, which in turn influence the width of the space charge region. In fact, a stronger electric field, responsible for the better charge separation observed among the pristine electrodes, is expected in the thinner with respect to the thicker electrode, since a

similar voltage drop occurs over a smaller distance. On the other hand, after H_2-treatment any relevant further gain in electric field under polarization of the thinner ZFO_70@800 film is prevented by the narrowing of the depletion region caused by the increase in donor density, according to PEIS analyses (see Section 3.4).

Therefore, H_2 treatment performed on the more crystalline films prepared at 800 °C enhances their bulk charge separation up to a maximum value regardless of the film thickness, beyond which the performance of the electrodes is ultimately governed by their photon absorption capability. A different behaviour is observed for the less crystalline samples calcined at 600 °C, with an increase in η_{sep} upon H_2 treatment for the thinner film of the series only.

3.4 Electrochemical Impedance Spectroscopy

Electrochemical impedance spectroscopy experiments were conducted under standard water oxidation conditions (1-Sun illumination, 1.0 M NaOH electrolyte) in back-side configuration, on the ZFO_70@600 and ZFO_160@800 films, in both pristine and hydrogen-treated forms. The PEIS data were fitted to a modified Randles circuit, consisting of a series resistance R_S, a bulk capacitance C_{bulk} such that $C_{bulk}^{-1} = C_{SC}^{-1} + C_H^{-1}$, where C_{SC} is the space charge layer capacitance and C_H the Helmholtz capacitance, a parallel resistance of hole trapping to surface states R_{trap}, a surface state capacitance C_{SS} and a charge transfer resistance from surface states to oxidize water $R_{ct,SS}$. The Mott-Schottky (M-S) plots for the investigated electrodes, constructed with the values of C_{SC} plotted as a function of the applied potential, are shown in **Figure S7**.

The fitting parameters, *i.e.* the donor density values N_D and the flatband potential E_{FB} calculated from the slope and extrapolated from the abscissa-intercept of each M-S plot, respectively, are reported in **Table 2**, together with the space charge layer width (W) at 1.5 V *vs.* RHE, calculated according to the following equation:[65]

$$W = \sqrt{\frac{2\varepsilon\varepsilon_0}{qN_D}|E - E_{FB}|} \quad \#(2)$$

where ε is the dielectric constant of ZFO, ε_0 is vacuum permittivity and q is elementary charge. Data relative to both pristine ZFO_70@600 and hydrogen-treated H_2 ZFO_70@600 are omitted in Table 2 since the M-S model could not be applied to these films (illogical values were obtained for the M-S plot reported in **Figure S7a**).

Table 2. Flatband potential, E_{FB}, and donor density, N_D, values calculated from M-S analyses and space charge width, W, calculated from equation (2).

Sample	E_{FB} / V_{RHE}	N_D / cm^{-3}	W @ 1.5 V_{RHE} / nm
ZFO_160@800	0.80	$1.7 \cdot 10^{18}$	70
H_2 ZFO_160@800	0.80	$2.7 \cdot 10^{19}$	17

The extrapolated flatband potential is in good accordance with the photocurrent onset potentials of the *J-V* plots reported in **Figure 3**. The one order of magnitude N_D increase attained upon H_2-treatment of the more crystalline ZFO_160@800 film compared to its pristine form clearly suggests that an increase in donor density is provided by H_2-treatment, demonstrating its n-type character, able to enhance the electron conductivity of the films.

From the measured donor density values, a reduction of the space charge layer width from 70 to 17 nm can be detected upon H_2-treatment of the ZFO_160@800 sample, according to **Eq. 2**. Although the estimation of W for the pristine ZFO_70@600 film is not possible, it is reasonable to guess that a decrease in W might have occurred also upon H_2-treatment of the less crystalline sample.

4. Discussion

Merging the results obtained through PEC measurements in the presence of the sacrificial agent with those of IMPS analyses conducted *in operando*, allows to interpret the photocurrent trends at 1.5 V *vs.* RHE reported in **Figure 2** in light of the obtained η_{sep} and η_{inj} trends.

The poor crystallinity induced by the lower preparation temperature clearly results in the presence of a large amount of both bulk and surface defects responsible for the low bulk charge separation and surface charge injection efficiencies of the less crystalline films annealed at 600 °C, in turn leading to their almost flat trend in photocurrent as a function of the film thickness (**Figure**

2a). Preparing the ZFO at higher temperature (800 °C) mainly improves the charge injection efficiency at the ZFO photoanode/electrolyte interface for any film thickness, likely through the deactivation of surface trapping states at this interface, as a consequence of the gain in film crystallinity according to PXRD analysis (**Figure S2**).[54]

While the same η_{inj} behaviour was observed for ZFO NR electrodes,[40] the charge transport in planar ZFO films should be primarily governed by the crystallinity of the material[66] rather than by the cation disorder, at difference with respect to ZFO NR as supported by the trends in d and δ shown in **Figure 1c**. A minor enhancement in charge separation with rising the synthesis temperature can be observed at low thickness only (**Figure 6b**), resulting in the photocurrent drop observed among the pristine electrodes prepared at 800 °C after the optimal 160 nm thickness (**Figure 2b**). This behaviour can be reasonably ascribed to the progressive increase in bulk resistance to charge transport and/or to the decreased effect of the built-in electric field generated in the space charge region with increasing thickness.

On the other hand, hydrogen treatment exerts its main impact on the charge separation efficiency, which underwent up to a 4-fold enhancement with best performing ZFO_240@800 after H_2-treatment (**Figure 6b**). This reflects the well-established doping effect of H_2-treatment, known to enhance the performance of metal oxide photoanodes through the introduction of oxygen vacancies acting as electron donors.[23,27,55,67] In this way, charge separation across the bulk of the film could benefit from the enhanced majority carrier density, since that will increase the built-in electric field across the space charge region[68] and enhance the film conductivity, both contributing to an improved electron transport.[27,55,67]

Hydrogen treatment improves charge separation at the various film thicknesses to a largely different extent depending on the initial ZFO synthesis temperature, being much more beneficial to the more crystalline films prepared at 800 °C (**Figure 2b**). Among them, a higher H_2-treatment efficiency in terms of a larger improvement in η_{sep} is attained when moving towards the thicker film of the series (**Figure 6b**), where the optimization of the charge separation in the thicker photoactive

layer combined with its superior absorption capability allows for the actual exploitation of a larger amount of photogenerated couples.

The reductive treatment applied on the poorly crystalline films induces a significant η_{sep} increase in the thinner electrode only, while a negligible improvement is observed with the hydrogen-treated thicker film compared to its pristine form (**Figure 6b**). This behaviour can be ascribed to the very poor crystallinity imparted by the lower preparation temperature, which hampers charge transport over thick films.

Minor effects, strongly dependent on both film thickness and synthesis temperature, were produced by H_2-treatment on the charge injection properties at the photoanode surface, as ascertained through both PEC measurements in the presence of the sacrificial agent and IMPS analyses.

The combined use of the higher 800 °C preparation temperature for effective surface charge injection and of hydrogen doping for an improved bulk charge transport is essential to maximize the performance of our planar ZFO films.

5. Conclusions

The interplay between synthesis temperature, film thickness and reductive H_2-treatment treatment onto the PEC performance of optically transparent planar ZFO photoanodes for water oxidation has been here elucidated. IMPS measurements performed *in operando* allowed to identify the role of the preparation temperature and hydrogen treatment separately onto the surface charge injection and bulk charge separation processes, as a function of the film thickness. The superior crystallinity of the electrodes prepared at higher temperature increases the performance of our ZFO pristine films and ensures an enhanced bulk charge separation upon H_2-treatment, though remaining below *ca.* 10% due to the intrinsic poor electronic conductivity of zinc ferrite material associated with a strong bulk recombination. The complementary roles played by the here-optimized synthesis parameters should be exploited to construct efficient ZFO photoanodes to be implemented in PEC tandem cells where planar geometry is an important requirement for high optical film transparency.

Acknowledgements

The authors thank Dr. P.A. Schouwink (EPFL) for support with XRD measurements. This research was partially funded by the MIUR PRIN 20173397R7 MULTI-e project, and by the Swiss National Science Foundation (SNSF) under the grant PZENP2_166871.

References

1 S. J. Davis, N. S. Lewis, M. Shaner, S. Aggarwal, D. Arent, I. L. Azevedo, S. M. Benson, T. Bradley, J. Brouwer, Y. M. Chiang, C. T. M. Clack, A. Cohen, S. Doig, J. Edmonds, P. Fennell, C. B. Field, B. Hannegan, B. M. Hodge, M. I. Hoffert, E. Ingersoll, P. Jaramillo, K. S. Lackner, K. J. Mach, M. Mastrandrea, J. Ogden, P. F. Peterson, D. L. Sanchez, D. Sperling, J. Stagner, J. E. Trancik, C. J. Yang and K. Caldeira, *Science*, 2018, **360** (6396), No. eaas9793.

2 D. G. Nocera, *Acc. Chem. Res.*, 2017, **50**, 616–619.

3 I. Roger, M. A. Shipman and M. D. Symes, *Nat. Rev. Chem.*, 2017, **1**, 0003/1–13.

4 J. H. Kim, D. Hansora, P. Sharma, J. W. Jang and J. S. Lee, *Chem. Soc. Rev.*, 2019, **48**, 1908–1971.

5 J. Qi, W. Zhang and R. Cao, *Adv. Energy Mater.*, 2018, **8**, 1–16.

6 Y. Dai, J. Yu, C. Cheng, P. Tan and M. Ni, *J. Mater. Chem. A*, 2020, **8**, 6984–7002.

7 S. D. Tilley, *Adv. Energy Mater.*, 2019, **9**, 1–13.

8 M. S. Prévot and K. Sivula, *J. Phys. Chem. C*, 2013, **117**, 17879–17893.

9 J. H. Kim, H. Kaneko, T. Minegishi, J. Kubota, K. Domen and J. S. Lee, *ChemSusChem*, 2016, **9**, 61–66.

10 C. Jiang, S. J. A. Moniz, A. Wang, T. Zhang and J. Tang, *Chem. Soc. Rev.*, 2017, **46**, 4645–4660.

11 C. R. Lhermitte, A. Polo, L. Yao, F. A. Boudoire, N. Guijarro and K. Sivula, *ChemSusChem*, 2020, **13**, 3645–3653.

12 T. Higashi, H. Nishiyama, Y. Suzuki, Y. Sasaki, T. Hisatomi, M. Katayama, T. Minegishi, K. Seki, T. Yamada and K. Domen, *Angew. Chemie - Int. Ed.*, 2019, **58**, 2300–2304.

13 J. H. Kim, J.-W. Jang, Y. H. Jo, F. F. Abdi, Y. H. Lee, R. van de Krol and J. S. Lee, *Nat. Commun.*, 2016, **7**, 13380/1–9.

14 K. Sivula, *J. Phys. Chem. Lett.*, 2013, **4**, 1624–1633.

15 K. Sivula and R. van de Krol, *Nat. Rev. Mater.*, 2016, **1**, 15010/1–16.

16 C. R. Lhermitte and K. Sivula, *ACS Catal.*, 2019, **9**, 2007–2017.

17 Y. Yang, S. Niu, D. Han, T. Liu, G. Wang and Y. Li, *Adv. Energy Mater.*, 2017, **7**, 1700555/1–26.

18 D. K. Lee, D. Lee, M. A. Lumley and K.-S. Choi, *Chem. Soc. Rev.*, 2019, **48**, 2126–2157.

19 F. F. Abdi and S. P. Berglund, *J. Phys. D. Appl. Phys.*, 2017, **50**, 193002/1–22.

20 F. E. Osterloh, *Chem. Soc. Rev.*, 2013, **42**, 2294–2320.

21 R. Dillert, D. H. Taffa, M. Wark, T. Bredow and D. W. Bahnemann, *APL Mater.*, 2015, **3**, 104001/1–15.

22 L. G. J. de Haart, *J. Electrochem. Soc.*, 1985, **132**, 2933–2938.

23 N. Guijarro, P. Bornoz, M. Prévot, X. Yu, X. Zhu, M. Johnson, X. Jeanbourquin, F. Le Formal and K. Sivula, *Sustain. Energy Fuels*, 2018, **2**, 103–117.

24 J. H. Kim, H. E. Kim, J. H. Kim and J. S. Lee, *J. Mater. Chem. A*, 2020, **8**, 9447–9482.

25 A. G. Hufnagel, K. Peters, A. Müller, C. Scheu, D. Fattakhova-Rohlfing and T. Bein, *Adv. Funct. Mater.*, 2016, **26**, 4435–4443.

26 J. H. Kim, J. H. Kim, J.-W. Jang, J. Y. Kim, S. H. Choi, G. Magesh, J. Lee and J. S. Lee, *Adv. Energy Mater.*, 2015, **5**, 1401933/1–9.

27 J. H. Kim, Y. J. Jang, J. H. Kim, J. W. Jang, S. H. Choi and J. S. Lee, *Nanoscale*, 2015, **7**, 19144–19151.

28 J. H. Kim, Y. J. Jang, S. H. Choi, B. J. Lee, J. H. Kim, Y. Bin Park, C.-M. Nam, H. G. Kim and J. S. Lee, *J. Mater. Chem. A*, 2018, **6**, 12693–12700.

29 Y. Guo, N. Zhang, X. Wang, Q. Qian, S. Zhang, Z. Li and Z. Zou, *J. Mater. Chem. A*, 2017, **5**, 7571–7577.

30 J. H. Kim, Y. J. Jang, S. H. Choi, B. J. Lee, M. H. Lee and J. S. Lee, *ACS Sustain. Chem. Eng.*, 2019, **7**, 944–949.

31 W. Gao, R. Peng, Y. Yang, X. Zhao, C. Cui, X. Su, W. Qin, Y. Dai, Y. Ma, H. Liu and Y. Sang, *ACS Energy Lett.*, 2021, 2129–2137.

32 J. H. Kim, J. H. Kim, J. H. Kim, Y. K. Kim and J. S. Lee, *Sol. RRL*, 2020, **4**, 1900328–1900338.

33 Y. Liu, M. Xia, L. Yao, M. Mensi, D. Ren, M. Grätzel, K. Sivula and N. Guijarro, *Adv. Funct. Mater.*, 2021, **31**, 2010081–2010088.

34 S. Kim, M. A. Mahadik, W. S. Chae, J. Ryu, S. H. Choi and J. S. Jang, *Appl. Surf. Sci.*, 2020, **513**, 145528–145544.

35 T. H. Jeon, G. hee Moon, H. Park and W. Choi, *Nano Energy*, 2017, **39**, 211–218.

36 J. Y. Kim, G. Magesh, D. H. Youn, J. W. Jang, J. Kubota, K. Domen and J. S. Lee, *Sci. Rep.*, 2013, **3**, 1–8.

37 A. A. Tahir and K. G. U. Wijayantha, *J. Photochem. Photobiol. A Chem.*, 2010, **216**, 119–125.

38 J. Wang, Y. Wang, X. Xv, Y. Chen, X. Yang, J. Zhou, S. Li, F. Cao and G. Qin, *Dalt. Trans.*, 2019, **48**, 11934–11940.

39 K. Kirchberg, S. Wang, L. Wang and R. Marschall, *ChemPhysChem*, 2018, **19**, 2313–2320.

40 X. Zhu, N. Guijarro, Y. Liu, P. Schouwink, R. A. Wells, F. Le Formal, S. Sun, C. Gao and K. Sivula, *Adv. Mater.*, 2018, **30**, 1801612/1–6.

41 A. Polo, C. R. Lhermitte, M. V. Dozzi, E. Selli and K. Sivula, *Surfaces*, 2020, **3**, 93–104.

42 W. Q. Hong, *J. Phys. D. Appl. Phys.*, 1989, **22**, 1384–1385.

43 S. Murcia-López, C. Fàbrega, D. Monllor-Satoca, M. D. Hernández-Alonso, G. Penelas-Pérez, A. Morata, J. R. Morante and T. Andreu, *ACS Appl. Mater. Interfaces*, 2016, **8**, 4076–4085.

44 Z. Wang, D. Schiferl, Y. Zhao and H. S. C. O'Neill, *J. Phys. Chem. Solids*, 2003, **64**, 2517–2523.

45 D. Peeters, D. H. Taffa, M. M. Kerrigan, A. Ney, N. Jöns, D. Rogalla, S. Cwik, H. W. Becker, M. Grafen, A. Ostendorf, C. H. Winter, S. Chakraborty, M. Wark and A. Devi, *ACS Sustain. Chem. Eng.*, 2017, **5**, 2917–2926.

46 K. Murugappan, D. S. Silvester, D. Chaudhary and D. W. M. Arrigan, *ChemElectroChem*, 2014, **1**, 1211–1218.

47 O. N. Shebanova and P. Lazor, *J. Solid State Chem.*, 2003, **174**, 424–430.

48 W. S. Bourée, M. S. Prévot, X. A. Jeanbourquin, N. Guijarro, M. Johnson, F. Le Formal and K. Sivula, *Adv. Mater.*, 2016, **28**, 9308–9312.

49 D. L. A. De Faria, S. Venâncio Silva and M. T. De Oliveira, *J. Raman Spectrosc.*, 1997, **28**, 873–878.

50 N. S. Chaudhari, S. S. Warule, S. Muduli, B. B. Kale, S. Jouen, B. Lefez, B. Hannoyer and S. B. Ogale, *Dalt. Trans.*, 2011, **40**, 8003–8011.

51 F. Bræstrup, B. C. Hauback and K. K. Hansen, *J. Solid State Chem.*, 2008, **181**, 2364–2369.

52 S. Bid and S. K. Pradhan, *Mater. Chem. Phys.*, 2003, **82**, 27–37.

53 C. N. Chinnasamy, A. Narayanasamy, N. Ponpandian, K. Chattopadhyay, H. Guérault and J. M. Greneche, *J. Phys. Condens. Matter*, 2000, **12**, 7795–7805.

54 O. Zandi and T. W. Hamann, *J. Phys. Chem. Lett.*, 2014, **5**, 1522–1526.

55 X. Zhao, J. Feng, S. Chen, Y. Huang, T. C. Sum and Z. Chen, *Phys. Chem. Chem. Phys.*, 2017, **19**, 1074–1082.

56 H. Dotan, K. Sivula, M. Grätzel, A. Rothschild and S. C. Warren, *Energy Environ. Sci.*, 2011, **4**, 958–964.

57 Y. Lan, Z. Liu, Z. Guo, M. Ruan and Y. Xin, *J. Colloid Interface Sci.*, 2019, **552**, 111–121.

58 N. Sato, *Electrochemistry at Metal and Semiconductor Electrodes*, Elsevier, Elsevier, edn. 1998.

59 D. Klotz, D. A. Grave and A. Rothschild, *Phys. Chem. Chem. Phys.*, 2017, **19**, 20383–20392.

60 E. A. Ponomarev and L. M. Peter, *J. Electroanal. Chem.*, 1995, **396**, 219–226.

61 D. Klotz, D. S. Ellis, H. Dotan and A. Rothschild, *Phys. Chem. Chem. Phys.*, 2016, **18**, 23438–23457.

62 F. Boudoire, Y. Liu, F. Le Formal, N. Guijarro, C. R. Lhermitte and K. Sivula, *J. Phys. Chem. C*, 2021, **125**, 10883–10890.

63 Y. Liu, F. Le Formal, F. Boudoire, L. Yao, K. Sivula and N. Guijarro, *J. Mater. Chem. A*, 2019, **7**, 1669–1677.

64 Y. Liu, F. Le Formal, F. Boudoire and N. Guijarro, *ACS Appl. Energy Mater.*, 2019, **2**, 6825–6833.

65 M. X. Tan, P. E. Laibinis, S. T. Nguyen, J. M. Kesselman, C. E. Stanton and N. S. Lewis, ed. John Wiley & Sons, 2007, pp. 21–144.

66 S. C. Warren, K. Voïtchovsky, H. Dotan, C. M. Leroy, M. Cornuz, F. Stellacci, C. Hébert, A. Rothschild and M. Grätzel, *Nat. Mater.*, 2013, **12**, 842–849.

67 M. Rioult, D. Stanescu, E. Fonda, A. Barbier and H. Magnan, *J. Phys. Chem. C*, 2016, **120**, 7482–7490.

68 M. S. Prévot, N. Guijarro and K. Sivula, *ChemSusChem*, 2015, **8**, 1359–1367.

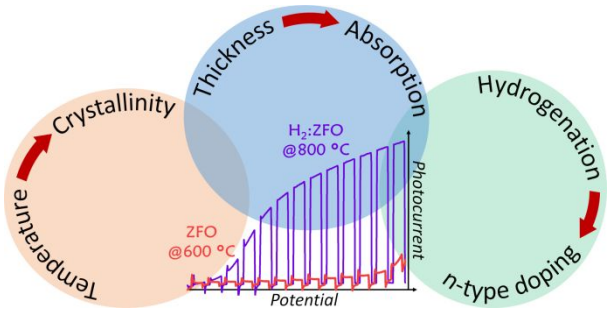

The interplay between a high film crystallinity and n-type doping in enhancing the performance of $ZnFe_2O_4$ photoanodes has been revealed in flat films with high optical transparency. Maximum benefit was achieved for the thickest photoactive layers with superior photon harvesting capability.

Journal of Materials Chemistry A

Manuscript ID: TA-ART-09-2021-007499

" Key factors boosting the performance of planar $ZnFe_2O_4$ photoanodes for solar water oxidation "

Authors: Polo, Annalisa; Boudoire, Florent; Lhermitte, Charles; Liu, Yongpeng; Guijarro, Néstor; Dozzi, Maria Vittoria; Selli, Elena; Sivula, Kevin

Response to Reviewers' comments and list of changes

Reviewer: 1

Comments to the Author

The manuscript from Sivula and coworkers examines planar $ZnFe_2O_4$ photoanodes fabricated via sol-gel processing for solar water oxidation. The group has published now a few papers on spinel ferrite photoelectrodes, including another study examining improvement of charge transport using post-synthetic H_2 treatment of planar $ZnFe_2O_4$ films fabricated via a different approach (doi: doi:10.3390/surfaces3010009). The present manuscript applies similar methodology to the article mentioned above, but with a different synthesis procedure and with the addition of intensity modulated photocurrent spectroscopy (IMPS) characterization. By moving to a sol-gel based approach, the authors are able to grow a wider range of film thicknesses that was not possible with their previous growth method. With this in mind, the authors examine the relationship between film thickness, H_2 treatment, and PEC performance, focusing on charge separation and charge injection efficiency.

Overall, the manuscript is not particularly novel, given the authors previously examined the effect of H2 treatment on planar $ZnFe_2O_4$ photoanodes. However, extending such measurements to additional film thicknesses has given some additional insight into the factors affecting $ZnFe_2O_4$ PEC performance. The methodology and conclusions appear to be generally sound, and the work could be useful for other researchers working in the field. Therefore, I recommend publication if a few points can be addressed satisfactorily:

Authors' reply

We thank Reviewer 1 for having carefully evaluated our manuscript and for recognizing the new insights of the present study compared to previous one.

1) The authors should plot and include the linear voltammograms measured in hole scavenger (Na_2SO_3) solutions (in the dark and under illumination or alternatively with chopped light).

Authors' reply

The LSV plots recorded in a 1.0 M NaOH solution containing 0.5 M Na_2SO_3 under steady illumination and in the dark, shown below, are now included also in Figure S5 of the ESI file.

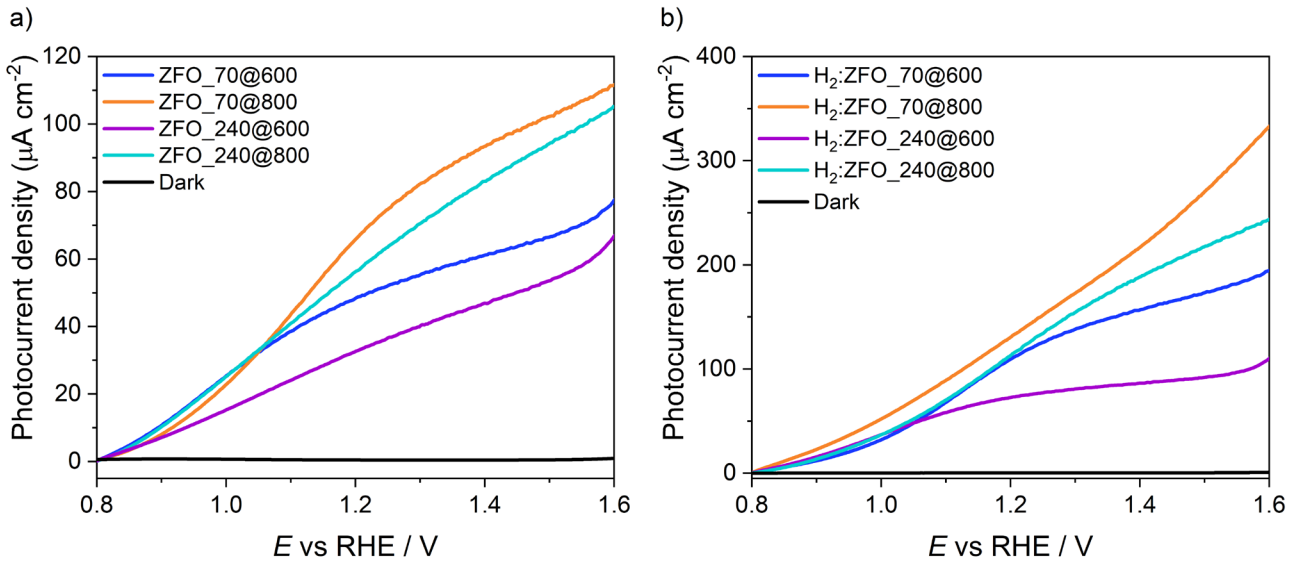

Linear Sweep Voltammetry (LSV) plots recorded in 1.0 M NaOH electrolyte solution containing 0.5 M Na_2SO_3 under back-side steady irradiation for the 70 nm and 240 nm-thick films annealed at either 600 °C or 800 °C, either before (a) or (b) after 1 h-long H_2-treatment.

2) Why is a peak observed in the charge injection efficiency at ~0.8 V_{RHE} for all the samples? I would expect charge injection efficiency only to increase with potential

Authors' reply

We thank Reviewer 1 for his/her insightful comment. The peak at 0.8 V_{RHE}, present in all η_{inj} plots regardless of the annealing temperature and the application of the post-synthesis treatment in H_2 atmosphere, is due to a non-zero capacitive current at the open circuit potential in our J-V curves recorded at a 20 mV s^{-1} scan rate. The charge injection efficiency plots, obtained by taking into account this contribution, are now reported in the new Figure 4 of the revised manuscript.

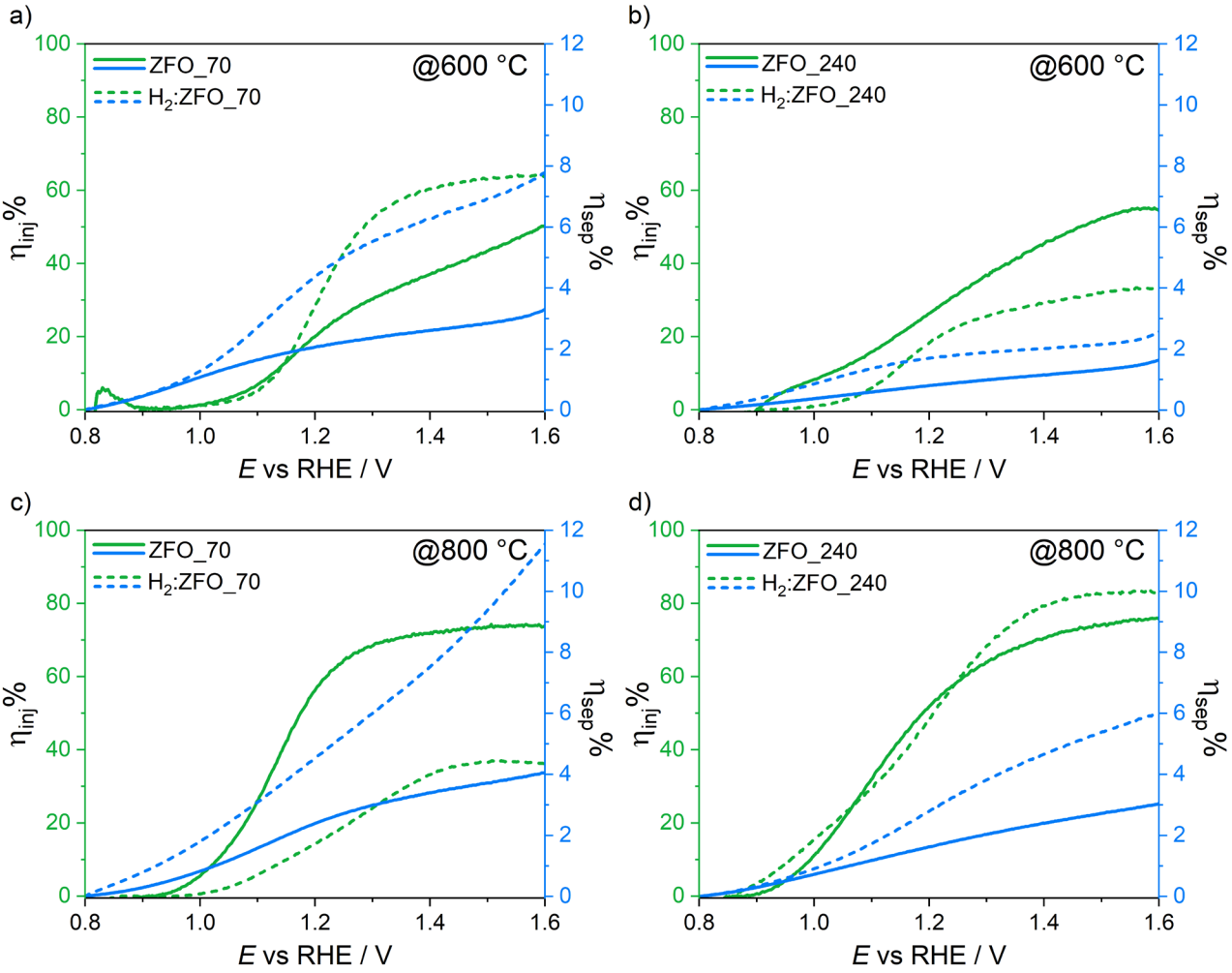

Charge injection (η_{inj}, green) and charge separation (η_{sep}, blue) efficiencies of the 70 nm and 240 nm-thick films prepared at either (a,b) 600 °C or (c,d) 800 °C, before (continuous lines) and after 1 h-long H_2-treatment (dashed lines).

3) Can the authors comment on the stability of the photoelectrodes?

Authors' reply

ZFO photoanodes and, more generally, spinel ferrites class to which this material belongs, stand out for the long-term photostability as well as for the remarkable thermal and chemical stability. In line with this, the ZFO planar photoelectrodes presented in this work exhibit outstanding stability as demonstrated by the good reproducibility of the tests carried out after several months. An example is reported below:

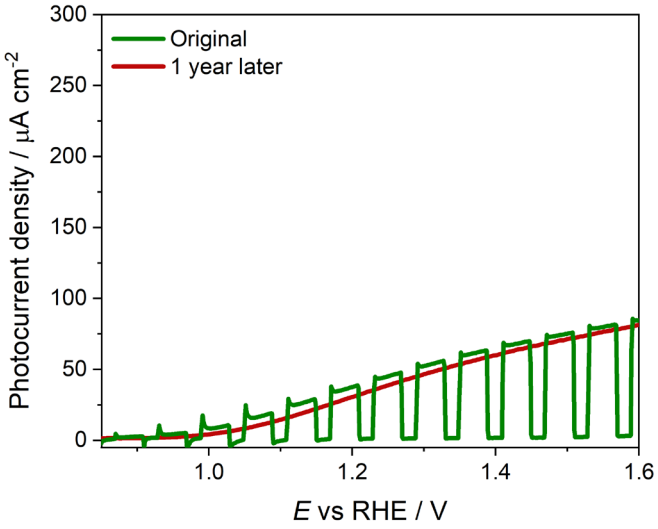

Comparison between LSV plots recorded with ZFO_240@800 in 1.0 M NaOH under back-side irradiation, at different times.

However, since this data is beyond the scope of the current report we do not include the above figure in the revised manuscript. Indeed, stability has been addressed in other works.

4) Given the high temperature heat treatment, has Sn diffusion from the FTO substrate been considered?

Authors' reply

Yes, annealing treatment at around 800 °C can trigger the diffusion of Sn^{4+} from the FTO substrate in hematite photoanodes, thus improving its activity for water oxidation (*J. Mater. Chem.*, 2012, **22**, 23232–23239, doi: 10.1039/c2jm34639g). Thus, a beneficial *n*-doping effect of Sn^{4+} on the performance of our planar ZFO photoanodes annealed at the higher 800 °C temperature cannot be discarded, in line with what was already observed for ZFO NR photoanodes undergoing the same annealing treatment (*Sustainable Energy Fuels*, 2018, **2**, 103–117, doi: 10.1039/C7SE00448F). This effect, which, together with the higher crystallinity, is already represented in the performance of pristine films (prior to H_2 treatment, see Figure 2b vs Figure 2a). The pristine films have much less photocurrent than the H_2 treated films. So, while the effect of the diffusion of Sn^{4+} cannot be completely discarded and likely has a small effect on the performance, it is negligible compared to effect of the H_2 treatment. To be clear to the reader about this, we have modified the main text to read "the higher crystallinity of the films prepared at 800 °C, and likely the diffusion of Sn^{4+} dopant from the FTO substrate[23], correlated to a higher activity of the pristine electrodes," on Page 12.

5) The authors should discuss how their results compare with the major result from the previous manuscript mentioned above, in which it was found that H_2 treatment improves the photoanode performance for films pre-annealed at lower temperatures, but not at higher temperatures. This appears to be consistent with 70@600 and 70@800 photoanodes in this work, but should be compared.

Authors' reply

We thank Reviewer 1 for this comment. The results presented in our previous paper (doi: doi:10.3390/surfaces3010009) refer to *ca.* 100 nm electrodes and are consistent with the actual ones obtained with electrodes of similar thickness, *i.e.* ≤ 100 nm. A different efficiency of hydrogen treatment in films pre-annealed at the two temperatures is here observed for higher film thicknesses.

This behavior is strictly correlated to our finding that charge transport in planar ZFO films is primarily governed by the crystallinity of the material. According to our discussion on page 12-13 of the manuscript, the thicker films of the more crystalline series benefit from the enhanced majority carrier density upon H_2-treatment, leading to the largest improvement in charge separation across the bulk of the film, as main effect of H_2 treatment. In contrast, the lower increase in η_{sep} exhibited by films thinner than 100 nm within the 800 °C electrodes series should be ascribed to the lack of a consistent gain in electric field when polarizing the thinner films after hydrogenation, due to the narrowing of the depletion region caused by the increased donor density. On the other hand, the very poor crystallinity imparted by the lower 600 °C pre-annealing temperature prevents charge transport in films thicker than 100 nm from benefiting from the reductive treatment.
A comparison with the results of our previous paper has been now added on page 13 of the revised manuscript, lines 4-7.

Reviewer: 2

Comments to the Author

In this manuscript, the authors report the key factors boosting the performance of planar ZFO photoanodes for solar water oxidation, i.e. the film preparation temperature and post-treatment in reductive environment. They have comprehensively investigated and compared the effect of sample preparation temperature, film thickness, and H_2 treatment on the photocurrent density, onset, charge inject efficiency and charge separation efficiency, providing insights into the correlation between PEC performance and sample preparation conditions. The reviewer would like to recommend the Editor to accept the manuscript for publication after minor revisions as noted below:

Authors' reply

We thank Reviewer 2 for having appreciated the exhaustivity of our investigation.

1. There are some diffraction peaks in Figure 1a that can be indexed as neither FTO nor ZFO. Can authors clarify where they are from?

Authors' reply

A more complete indexing, also reported in the ZFO diffractogram below, is now shown in Figure 1a of the new version of the manuscript, where the peaks at $2\Theta \sim 43°$ and 53°, indicative of the (400) and (422) crystal planes of the pure $ZnFe_2O_4$ phase, respectively, have been added. The presence of any other peak cannot be distinguished from background noise.

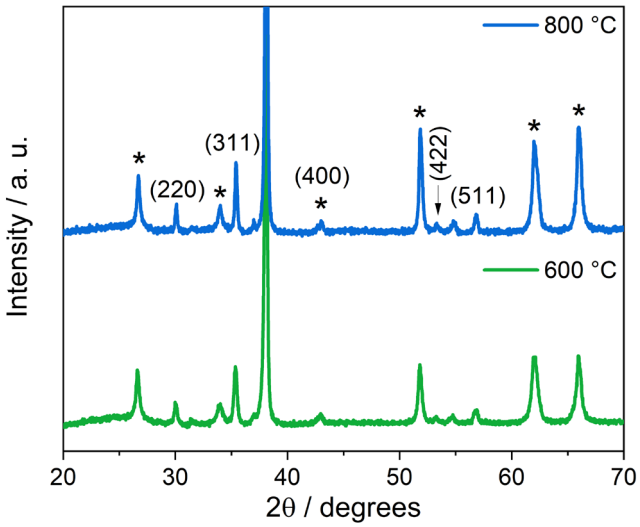

2. Abbreviations should be written out when they appear the first time in the manuscript, e.g. XRD, SEM, HV, SCLJ.

Authors' reply

We thank Reviewer 2 for his/her suggestion. Abbreviations have been now added where cited for the first time in the revised manuscript.

3. Can authors clarify why intermittent irradiation, instead of steady one, was used to record J-V?

Authors' reply

"Chopped light" photocurrent–voltage plots, where light and dark intervals are alternated, were recorded under intermittent irradiation as alternative to comparing the J-V curves acquired under continuous light illumination with those performed in the dark. Intermittent LSV plots point out even small differences between the dark current and the photocurrent, thus helping in determining the photocurrent onset potential accurately. This is common practice in the field.

4. Samples with ZFO thickness of 70 and 240 nm were used for LSV and IMPS measurements, but for EIS, sample series of ZFO_160 were used. Is there a special reason for using samples with different thickness?

Authors' reply

Samples with thickness of 70 nm and 240 nm—at the extremes of the investigated range—were employed both in IMPS and in the photocurrent density measurements using sacrificial conditions in order to compare the surface charge injection and charge separation efficiencies calculated through the two different methods (reported in Figures 4 and 6 of the manuscript), with the final aim of clarifying the observed trends in performance as a function of the film thickness (Figure 2). EIS data were instead presented for the sole purpose of evaluating the impact of hydrogenation on the flat-band potential, electron donor density, and space charge layer width values of our ZFO material. Therefore, an intermediate 160 nm thickness, already providing a significant effect of hydrogenation on the performance of the more crystalline series (see Figure 2b), was chosen as exemplary sample.

5. There are some minor grammatical errors to be corrected. For example,
1) Abstract: it should be "… combined effect … are investigated". In addition, please write out "PEC".
2) the first sentence, section 3.3: it should be "might not be"

Authors' reply

We thank Reviewer 2 for his/her observation. The minor grammatical errors have now been corrected in the revised manuscript.

Finally, we thank the Editor and both Reviewers for their positive comments. We hope that the revised version of the manuscript may now be accepted for publication in *Journal of Materials Chemistry A*.

Supporting Information

Key factors boosting the performance of planar $ZnFe_2O_4$ photoanodes for solar water oxidation

Annalisa Polo[a], Florent Boudoire[b], Charles R. Lhermitte[b], Yongpeng Liu[b], Néstor Guijarro[b], Maria Vittoria Dozzi[a], Elena Selli[a] and Kevin Sivula[b]

[a]*Dipartimento di Chimica, Università degli Studi di Milano, via Golgi 19, I-20133 Milano, Italy.*

[b]*Laboratory for Molecular Engineering of Optoelectronic Nanomaterials, École Polytechnique Fédérale de Lausanne (EPFL), Station 6, 1015 Lausanne, Switzerland.*

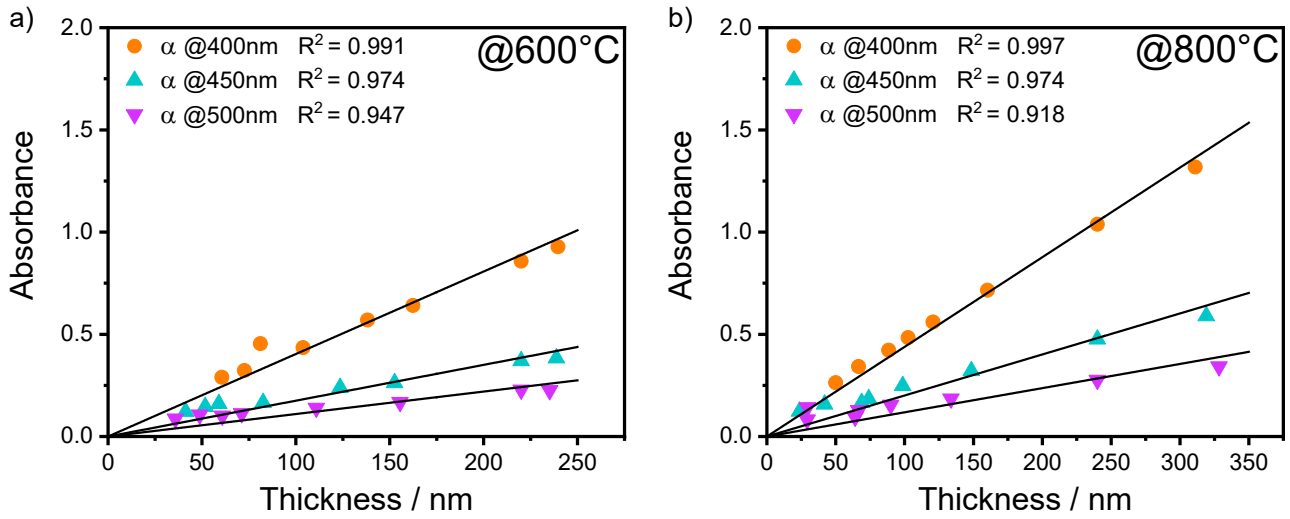

Figure S1. Absorbance at selected wavelengths vs. the film thickness for (a) the 600 °C and (b) the 800 °C films series. Absorbance (A) has been calculated as $A = 2 - \log(T\%)$ with $T\%$ referring to the percent transmittance. The best linearity was found for $\lambda = 400$ nm in both cases, with absorption coefficient values $\alpha_{600} = 0.0085$ nm^{-1} and $\alpha_{800} = 0.0093$ nm^{-1}.

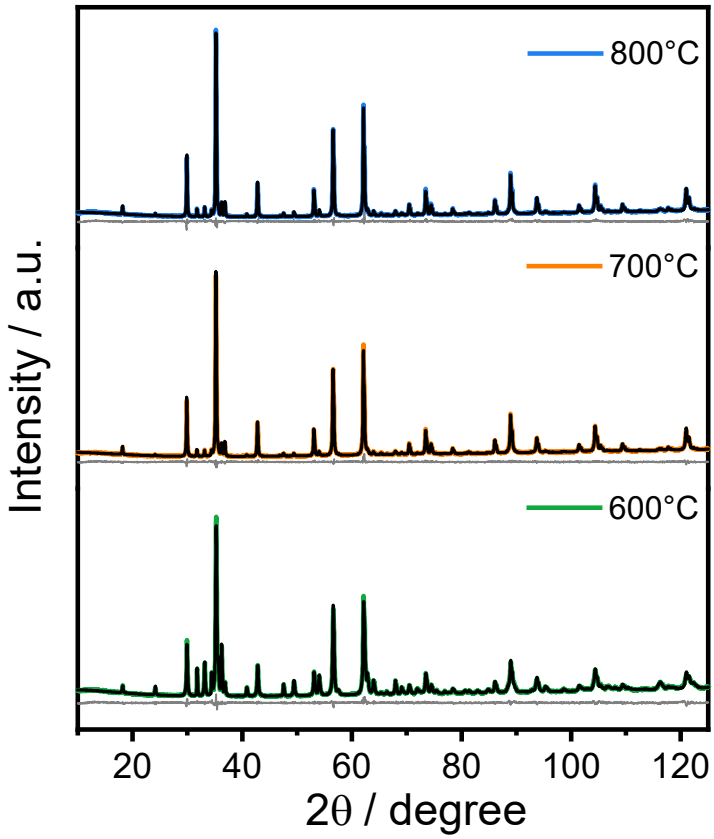

Figure S2. Rietveld refinement on PXRD of ZFO samples prepared at different temperatures. The coloured trace is the experimental pattern, the superimposed black trace is the fit Rietveld refinement and the grey trace below each pattern is the corresponding residual**.**

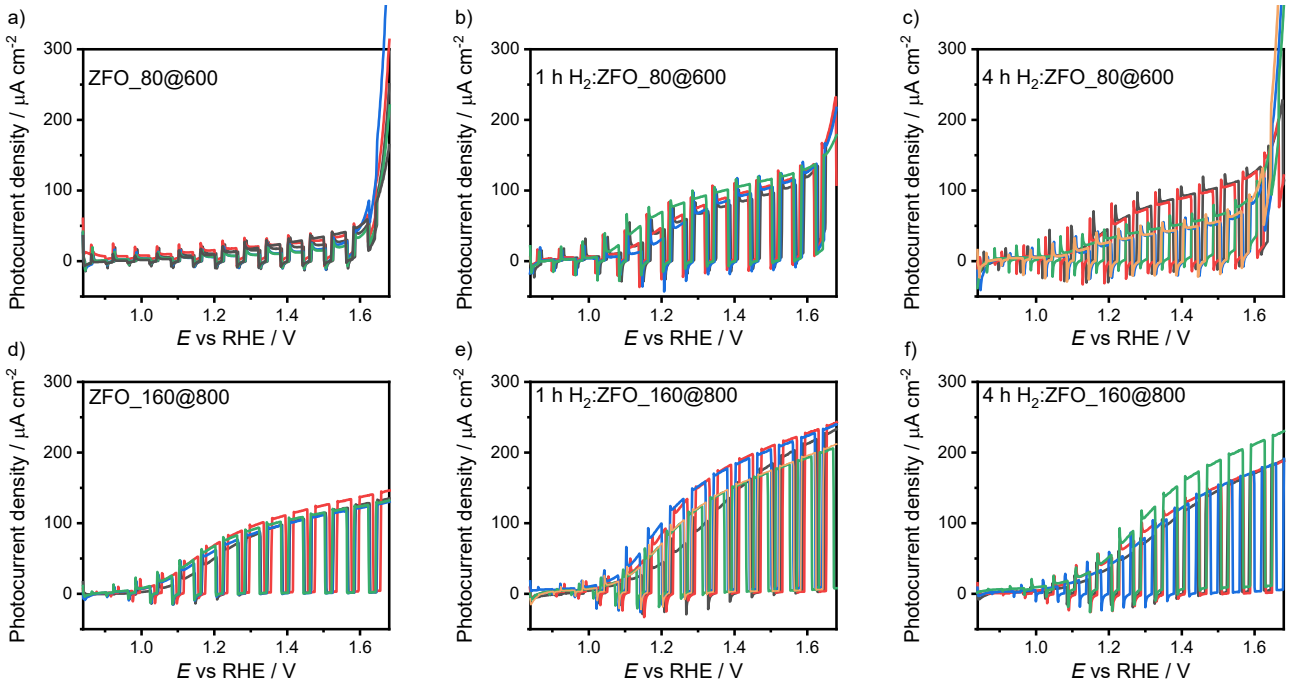

Figure S3. *J-V* curves reproducibility for representative samples of the two series, the 80 nm- and 160 nm-thick films calcined at 600 °C or 800 °C, respectively. The LSV plots were recorded with the two films (a,d) in their pristine form, (b,e) after 1 h-long hydrogenation and (c,f) after 4 h-long hydrogenation, in 1.0 M NaOH electrolyte solution under back-side irradiation.

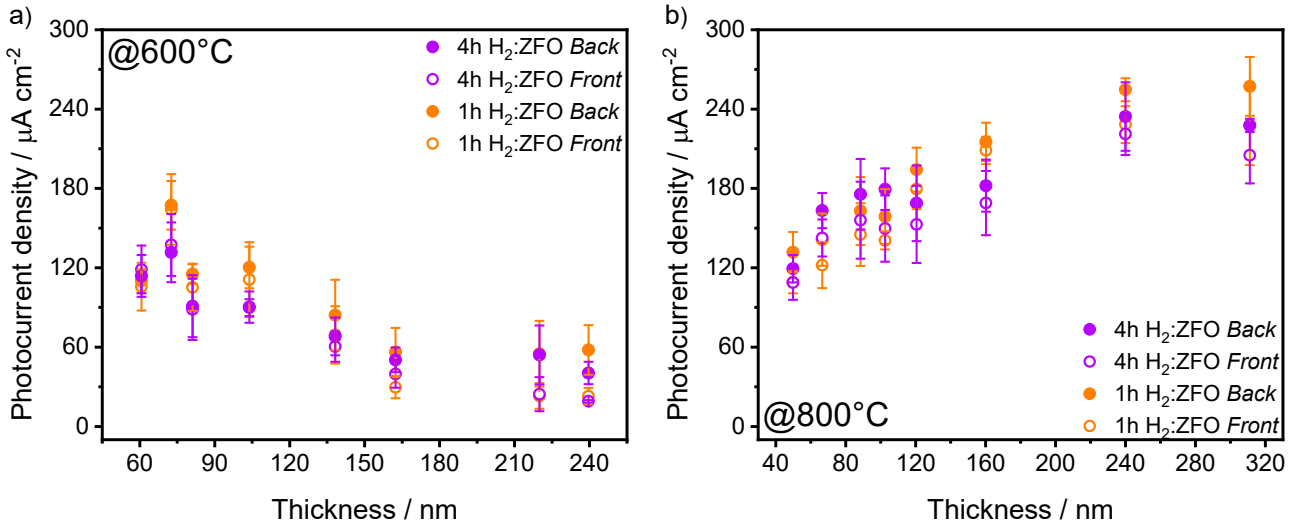

Figure S4. Photocurrent density *(J)* values at 1.5 V *vs.* RHE recorded with the films prepared at (a) 600 °C and (b) 800 °C after 1 h- (orange) and 4 h-long hydrogen treatment (violet), *vs.* the film thickness. *J* values were collected in 1.0 M NaOH solution under either back- (full circles) or front-side (void circles) irradiation.

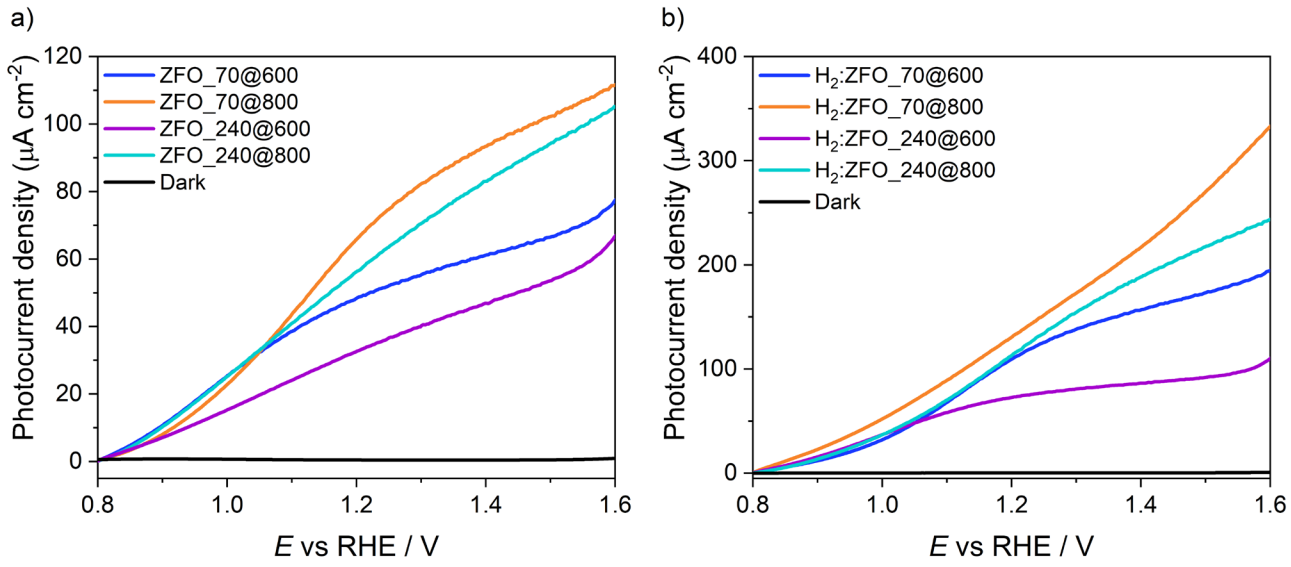

Figure S5. *J-V* curves recorded in 1.0 M NaOH electrolyte solution containing 0.5 M Na_2SO_3 under back-side irradiation for the 70 nm and 240 nm-thick films annealed at either 600 °C or 800 °C, either before (a) or (b) after 1 h-long H_2-treatment.

Intensity modulated photocurrent spectroscopy measurements

The IMPS response was fit to a phenomenological model,[1,2] according of the following equation:[3]

$$J(\omega) = \frac{J_h}{1 + (i\omega\tau_h)^{\alpha_1}} - \frac{J_r}{1 + (i\omega\tau_r)^{\alpha_2}} \quad \text{(S1)}$$

From the aforementioned fit model, the following parameters can be extrapolated: the bulk hole available for water oxidation (J_h) and the photocurrent losses due to surface recombination (J_r), and two time constants for bulk hole current (τ_h) and for surface recombination (τ_r). The non-ideality factor indicated as α_1 and α_2, used to describe the deformation of the semicircles due to frequency dependence dielectric constant, were selected to be close to 1.

The so derived parameters at 1.5 V *vs.* RHE, for each of the 8 compared films, are shown in **Figure S6**.

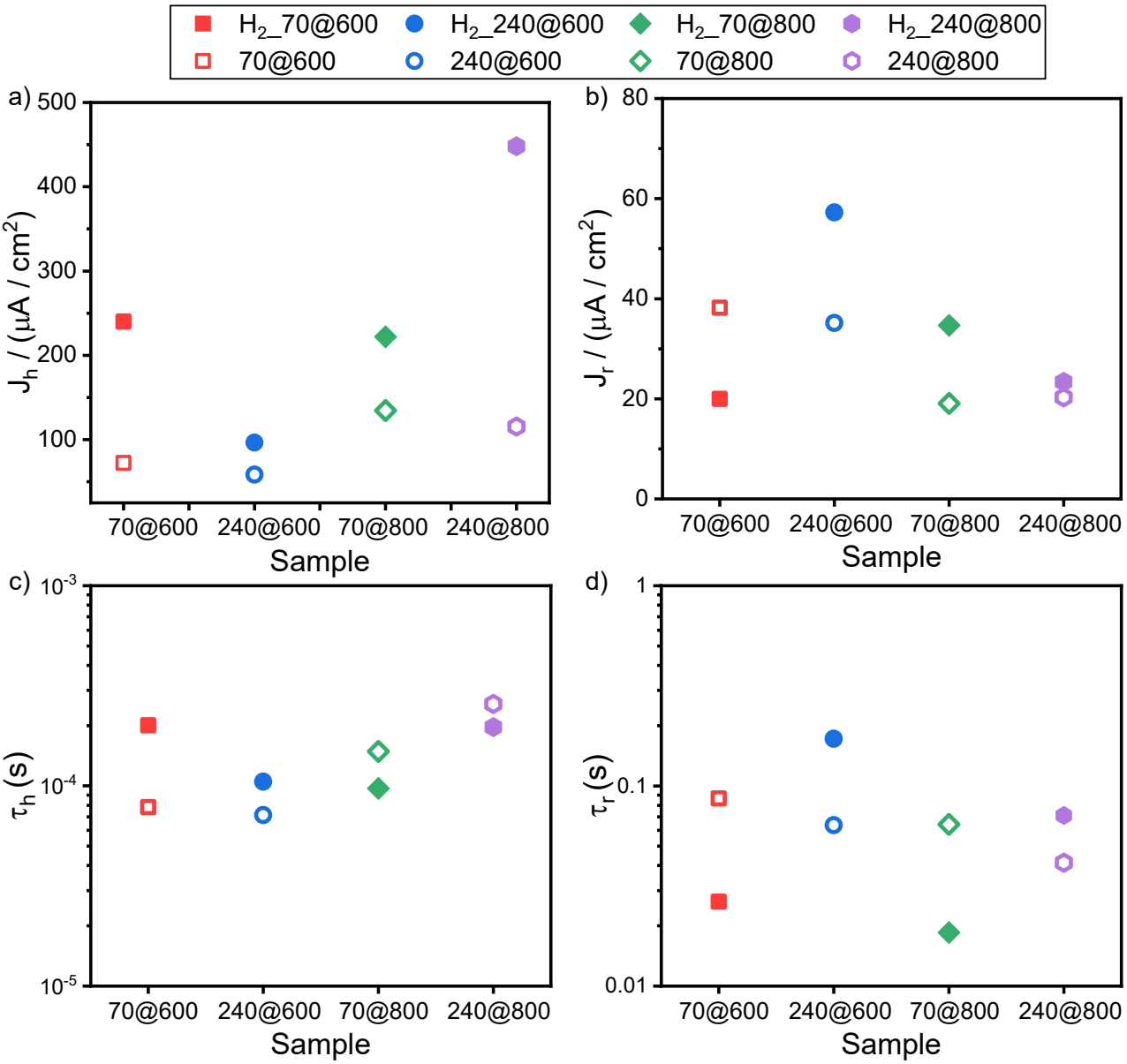

Figure S6. Extracted IMPS fit model parameters at 1.5 V *vs.* RHE for the 70 nm- and 240 nm-thick films calcined at either 600 °C or 800 °C: (a) bulk photocurrent available for water oxidation (J_h), (b) photocurrent losses due to surface recombination (J_r) and time constants for (c) bulk hole current (τ_h) and (d) for surface recombination (τ_r).

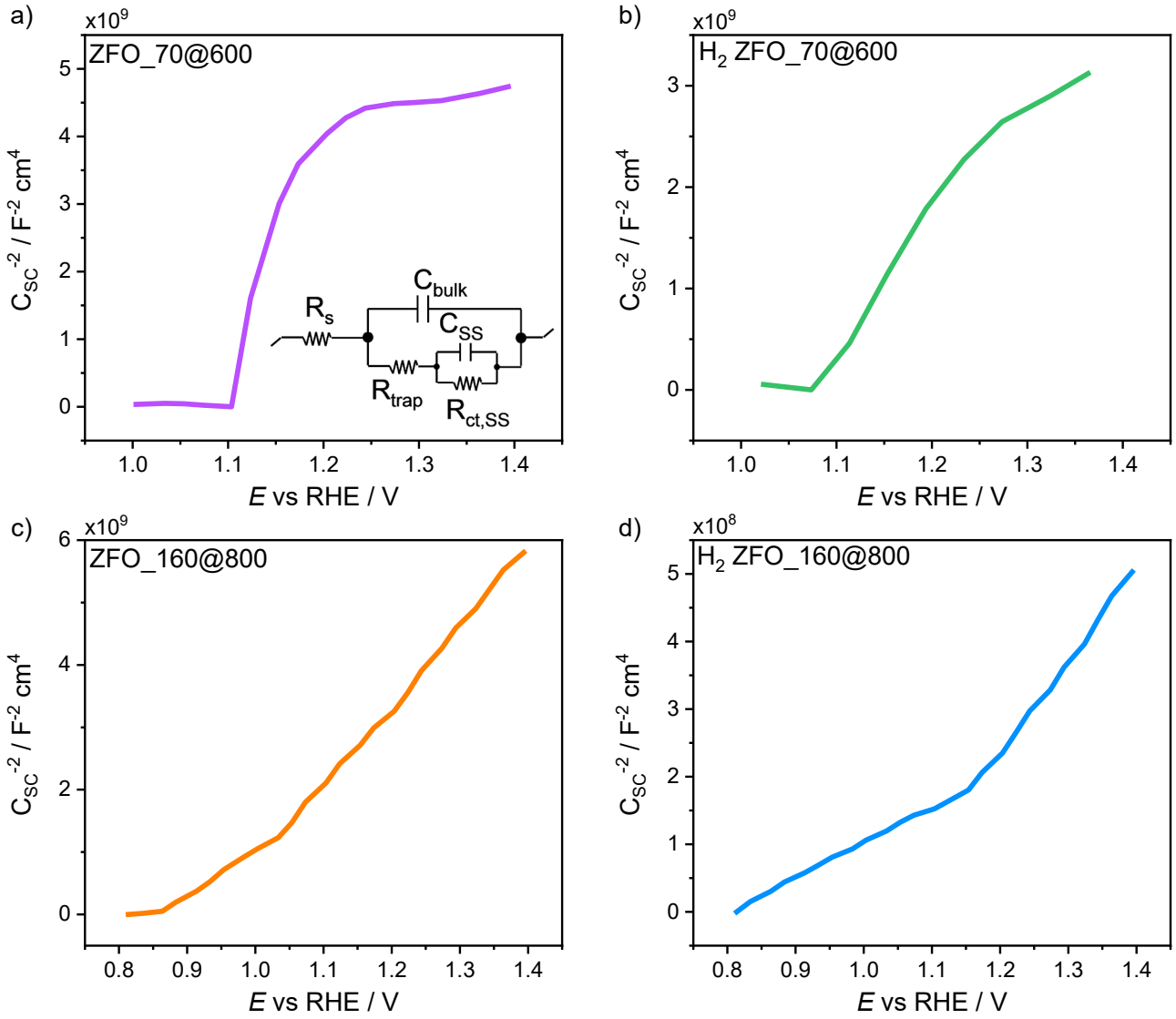

Figure S7. Mott-Schottky plots obtained with (a,b) ZFO_70@600 and (c,d) ZFO_160@800 films in their (a,c) pure and (b,d) hydrogenated forms, from PEIS measurements carried out in 1.0 M NaOH under AM 1.5 G solar simulated irradiation.

References

1 D. Klotz, D. S. Ellis, H. Dotan and A. Rothschild, *Phys. Chem. Chem. Phys.*, 2016, **18**, 23438–23457.

2 D. Klotz, D. A. Grave and A. Rothschild, *Phys. Chem. Chem. Phys.*, 2017, **19**, 20383–20392.

3 F. Boudoire, Y. Liu, F. Le Formal, N. Guijarro, C. R. Lhermitte and K. Sivula, *J. Phys. Chem. C*, 2021, **125**, 10883–10890.

Key factors boosting the performance of planar $ZnFe_2O_4$ photoanodes for solar water oxidation

Annalisa Polo[a], Florent Boudoire[b], Charles R. Lhermitte[b], Yongpeng Liu[b], Néstor Guijarro[b], Maria Vittoria Dozzi[a], Elena Selli[a] and Kevin Sivula[b]

[a]*Dipartimento di Chimica, Università degli Studi di Milano, via Golgi 19, I-20133 Milano, Italy*

[b]*Laboratory for Molecular Engineering of Optoelectronic Nanomaterials, École Polytechnique Fédérale de Lausanne (EPFL), Station 6, 1015 Lausanne, Switzerland*

Abstract

The performance of $ZnFe_2O_4$ photoanodes largely depends on their nanostructure, crystallinity and n-type doping, though decoupling their impact on photoactivity remains a challenge. Herein, the combined effects of the synthesis temperature and a reductive annealing post-treatment on the photoelectrochemical performance of planar $ZnFe_2O_4$ photoanodes are investigated in relation to a comprehensive range of film thickness, enabled by an optimized sol-gel synthetic approach. By eliminating the effects of nanostructure, a synergistic effect is revealed between the material crystallinity, controlled by synthesis temperature, and the n-type doping triggered by the H_2-treatment, which is maximum for the thickest photoactive layers. Intensity modulated photocurrent spectroscopy measurements performed *in operando* evidence the crucial impact of the synthesis temperature and the reductive treatment in inducing an effective surface charge injection and improved bulk charge transport, respectively, to enhance the photoelectrochemical performance of planar $ZnFe_2O_4$ films.

1. Introduction

Capturing and storing sunlight, the most plentiful renewable energy source, as chemical fuels in order to mitigate its intermittent and unpredictable nature, remains a key challenge towards realizing a fossil fuel-free, sustainable energy society.[1–3] Hydrogen (H_2) is a leading candidate as a clean fuel since it can be produced from water by solar-driven electrolysis.[4,5] A promising route in

this regard is photoelectrochemical (PEC) water splitting where direct semiconductor–liquid junctions (SCLJ) are used to drive the oxidation and reduction of water into O_2 and H_2, on a photoanode and a photocathode, respectively.[6,7] In principle a PEC tandem cell, where two complementary photoelectrodes are stacked to maximize the light harvesting efficiency, is a powerful strategy to enable unassisted and high efficiency solar water splitting.[8–10] However, realizing both high solar-to-hydrogen conversion efficiencies and robust device performance with this configuration has been limited by the development of semi-transparent semiconductor photoelectrodes with suitable band gap energy, high PEC activity, and stable performance.[8,11–13]

Indeed, identifying semiconducting materials for photoanodes that are capable of oxidizing water into oxygen with high efficiency and long-term stability is the major performance bottleneck of these devices. Metal oxide-based photoanodes stand out as promising candidates towards this aim, since they possess key requirements, such as low-cost, earth abundance, easily scalable processability, long-lasting durability under operation conditions and sufficiently oxidizing valence band maxima.[11,14–17] Several binary and ternary transition metal oxides, such as TiO_2, WO_3, $BiVO_4$ and Fe_2O_3, have been extensively studied, but their relatively wide band gap and/or poor semiconducting properties limit their practical application.[18–20] Therefore, the search for new ternary and multinary oxides able to absorb a large fraction of the solar spectrum and efficiently drive the oxygen evolution reaction (OER) remains an urgent need.[18]

In this regard, the spinel ferrite phases formed by ternary oxide compounds of iron(III) and a divalent metal (MFe_2O_4), have recently gained increasing interest for their excellent thermal and chemical stability. Moreover, the possibility to tune their band gap energy (1.4–2.1 eV) by selecting the divalent *M* cation (*M* = Zn, Mg, Cu, Ca, etc.) allows for controlling light harvesting in the visible range.[21–24] Specifically, $ZnFe_2O_4$ (ZFO) with a band gap energy of 2.0 eV has become a model system of this class of materials, as it shares many advantages of the well-studied hematite (Fe_2O_3) in addition to a 200 mV more negative photocurrent onset potential, which potentially allows for improved operation of a tandem cell.[19,25] However, the performance of ZFO photoanodes[25–34] remains far below

that of benchmark set by Fe_2O_3.[35,36] Detailed investigations revealed that a strong bulk recombination associated with a poor electron conductivity is a main issue with ZFO.[23,33,37,38] This limitation may be related to the extremely high temperature required to crystallize this class of materials.[26,27,39]

A post-synthesis thermal treatment under mild reductive conditions (*e.g.* under H_2 gas at 200 °C) is known to improve the conductivity of ZFO photoelectrodes through the introduction of oxygen vacancies acting as n-type dopants, thus increasing the majority carrier density of the material.[23,27,28,38,40,41] The reductive treatment of nanostructured ZFO films with a nanorod (NR) morphology led to a benchmark photocurrent density for solar water oxidation, and also pointed out that cation-site disorder may enhance the majority carrier transport in these electrodes even more than the film crystallinity, resulting in a superior separation of photogenerated charges.[40] However, although nanostructured architectures such as the NR morphology present many advantages for increasing charge collection efficiency (*e.g.* the channelized electron transport and reduced distance for minority charge carriers to reach the semiconductor/electrolyte interface), a detrimental light scattering side-effect compromises their use as top-layer photoanodes in PEC tandem devices.[11] Moreover, the NR morphology complicates decoupling and understanding the effects of the crystallinity and doping on the intrinsic material performance.

Accordingly, the development and optimization of ZFO films with a compact and planar geometry that simplifies the interpretation of the performance, and, due to their translucency, could also be more suitable in tandem cells is a recent research goal.[11,41] However, previous studies were limited by small film thickness (under 100 nm) due to the synthetic method employed. For this reason, in the present work we employ a modified sol-gel synthesis starting from a high precursor concentration to prepare planar ZFO films with different thickness, up to *ca.* 300 nm, in one single spin-coating deposition step. The PEC performance of these electrodes together with *in operando* intensity modulated photocurrent spectroscopy (IMPS) provide critical insight into the influence of the reductive hydrogen treatment on the fate of the photogenerated charges as a function of both the

film preparation temperature and the film thickness in the absence of morphological factors stemming from a nanostructured architecture.

2. Experimental Section

2.1 Chemicals and materials

The following chemicals were employed: $Zn(NO_3)_2 \cdot 6H_2O$ (ABCR), $Fe(NO_3)_3 \cdot 9H_2O$ (Acros Organics), NaOH (Reactolab SA) and Na_2SO_3 (Sigma-Aldrich). F-doped tin oxide (FTO) coated aluminoborosilicate glass (Solaronix) was used as conducting substrate.

2.2 Photoelectrode preparation

Thin $ZnFe_2O_4$ films with different thickness were prepared through the single-step spin-coating deposition of aqueous solutions containing different precursor concentrations, followed by a two-step heating procedure. The employed concentrations of the two metal nitrate precursors were determined in preliminary solubility tests, aiming at maximizing them while employing a suitable stoichiometry to obtain the desired phase. In this way, up to 40-fold higher nominal precursor concentrations were obtained with respect to those previously employed (*i.e.*, 0.25 M in Fe and 0.125 M in Zn).[11] All solutions were prepared with Millipore water (18.2 MΩ).

Prior to deposition, the FTO coated glass was thoroughly cleaned by sonication cycles in a soap/water mixture, acetone, ethanol, and finally in distilled water (15 min each) before plasma cleaning for 15 min. A static spin coating technique was used to deposit the precursor solution (150 μL) on the cleaned substrates, which were then spun at 500 rpm for 45 s. After spin coating, the films were first dried at 400 °C in air for 1 h, and then annealed in a tubular furnace preheated at 600 °C or 800 °C (for 20 min), followed by natural cooling to room temperature after switching the furnace off. Finally, the electrodes underwent a post-synthesis reductive treatment at 200 °C under a H_2 atmosphere for 1 h or 4 h. Powder samples for X-ray diffraction (XRD) analysis and Rietveld refinements (see next section) were prepared by annealing the precursor solutions at different temperature (600 °C, 700 °C and 800 °C) for 2 h.

2.3 Structural, morphological and optical characterizations

XRD data were collected using a Panalytical Empyrean system (Bragg-Brentano, 240 mm) equipped with a PIXcel-1D detector, a hybrid monochromator, and parallel beam optics. Raman spectra were recorded with a confocal Raman spectrometer (HORIBA Jobin Yvon XploRA PLUS) using a 532 nm wavelength laser for excitation. Powder X-ray diffraction (PXRD) analysis on the powder samples was conducted in a Bruker D8 Discover diffractometer using a non-monochromatized Cu-source, a Nickel filter and a LYNXEYE-XE energy-dispersive detector, which was set to filter Fe-fluorescence. Presented results were extracted from Rietveld refinements. Scanning electron microscope (SEM) data were collected using a Zeiss Gemini 300 scanning electron microscope in High Vacuum (HV) mode.

Transmittance and reflectance data were collected using a UV-3600 (Shimadzu) spectrometer equipped with an integrating sphere. The thickness of all synthesized films (reported in **Table 1**) was estimated using UV-Vis absorption and the estimated absorption coefficient α at the corresponding synthesis temperature. α values were calculated using the following equation:[42,43]

$$\alpha = -\frac{1}{h}\ln\left(\frac{T\%}{100 - R\%}\right) \#(1)$$

where h is the thickness (ca. 220-240 nm) of the reference sample for each synthesis temperature estimated from the cross-section SEM images (**Figure 1d**), *T%* and *R%* are the percent transmittance and reflectance values, respectively, of the same electrode at a selected wavelength. By comparing the linear regression plots, shown in **Figure S1**, of the absorbance at selected wavelengths *vs.* the estimated film thickness, $\lambda = 400$ nm was identified as the most suitable wavelength for α evaluation. The α values obtained according to **Eq. 1** for the two synthesis temperatures are $\alpha_{600}(400\text{ nm}) = 0.0085\text{ nm}^{-1}$ and $\alpha_{800}(400\text{ nm}) = 0.0093\text{ nm}^{-1}$.

2.4 Photoelectrochemical measurements

PEC measurements were carried out with a BioLogic SP-500 potentiostat connected to a cappuccino-type PEC cell (0.25 cm^2 active geometric area for the working electrode), in a three-

electrode configuration where a Ag/AgCl KCl (sat.) electrode and a Pt wire were used as reference and counter electrode, respectively. The light source was a 1000 W Xe arc lamp (Newport Oriel) calibrated using a Si photodiode to provide a photon flux corresponding to the AM 1.5 G spectrum (spectrally matched for $h\nu > 2.0$ eV). Intermittent-illumination linear sweep voltammetry (LSV) scans were acquired with a 20 mV s^{-1} scan rate by irradiating the electrode in both back (through the substrate-side) and front (through the electrolyte-side) configurations. The applied potentials acquired *vs.* Ag/AgCl in all measurements were converted to the reversible hydrogen electrode (RHE) using the equation: $E_{RHE} = E_{AgCl} + 0.059\ pH + 0.210$. LSV measurements were performed in either a 1.0 M NaOH aqueous electrolyte solution at pH 14, or in a 1.0 M NaOH solution containing also 0.5 M Na_2SO_3.

Photoelectrochemical impedance spectroscopy (PEIS) measurements were carried out in a 1.0 M NaOH electrolyte solution (pH 14) using a Bio-Logic SP-500 potentiostat coupled with the EC-Lab (V11.12) electrochemical platform. During each PEIS scan, the potential modulation frequency was scanned between 160 Hz and 50 mHz. A custom program written in the Python programming language was used to process and fit the PEIS data.

2.5 IMPS measurements and data analysis

IMPS tests were performed using a blue LED light generated by a customized light modulation system with 4 Cree XLamp MC-E LEDs. The sinusoidal modulation of the light intensity was controlled by a function generator (Tektronix AFG3021C), with a modulation depth of 10% and a frequency range from 80 kHz to 0.5 Hz. A three-electrode cappuccino-type cell was used, similar to that employed in the other PEC measurements. A Thompson Electrochem potentiostat (model 251) was used to control the applied potential on the working electrode and the photocurrent response was recorded by a digital oscilloscope (Tektronix DPO7254C) via a 50 Ω resistor (Velleman E6/E12) in series with a platinum counter electrode. IMPS data were processed and fitted using a custom program written in Igor Pro (WaveMetrics) and Origin Pro (OriginLab).

3. Results

To gain insight into the effect of the ZFO preparation temperature and the reductive hydrogen treatment on the photogenerated carrier transport and transfer, a series of planar ZFO electrodes was prepared using 8 different precursor concentrations, as reported in **Table 1**. The films obtained by spin coating the different precursor solutions were annealed at 600 °C or at 800 °C. Similar thickness values, determined by UV-vis absorption measurements (see Section 2.3), were obtained for the as-prepared ZFO films, independently of the synthesis temperature, as shown in **Table 1**.

Table 1. Adopted precursor solution concentrations and corresponding films thickness after heating at 600 or 800 °C.

[Fe^{3+}] / M	**[Zn^{2+}] / M**	**Thickness @ 600 °C / nm**	**Thickness @ 800 °C / nm**
0.5	0.25	60	50
1.0	0.5	70	70
1.5	0.75	80	90
2.0	1.0	100	100
2.5	1.25	140	120
5.0	2.5	160	160
7.5	3.75	220	240
10	5.0	240	310

Annealed films were directly employed in PEC measurements (coded as "pristine" samples) or underwent a further hydrogen treatment for 1 h or 4 h at 200 °C, to increase their carrier conductivity. All investigated ZFO electrodes are labelled as ZFO_X@Y, with X indicating the film thickness in nm, Y the annealing temperature in Celsius.

3.1 Structural, morphological and optical characterization

The phase composition and crystal structure of the as-prepared ZFO films were evaluated using XRD and Raman spectroscopy. Results obtained for the 160 nm-thick films annealed at 600 °C or 800 °C, are reported in **Figure 1**. The XRD patterns in **Figure 1a** only display the reflections

typical of cubic spinel $ZnFe_2O_4$ (JCPDS: 01-089-1010) and the diffraction peaks of SnO_2 associated to the FTO substrate (marked by asterisks). No signals for other segregated phases can be discerned. The peaks at about $2\theta = 30°$, 35.2°, 43°, 53° and 56.6° are indicative of the (220), (311), (400), (422) and (511) crystal planes, respectively, of the pure $ZnFe_2O_4$ phase, which crystallizes with a *Fd3m* space group.[23,26,38] The intensity of these reflections increases when the annealing temperature passes from 600 °C to 800 °C, which is an indication of the enhanced crystallinity of the films, in line with previous results on ZFO NR films.[40] Also, as established for ZFO NR films, the mild post-synthesis hydrogen treatment does not change the crystal structure.[23,26,27]

The Raman spectra over a wide range (100-1800 cm^{-1}) reported in **Figure 1b** further confirm the crystal phase and the absence of parasitic phases in the thin films prepared at 600 °C or 800 °C. In both cases, the weak feature appearing at 245 cm^{-1} and the three bands centred at 352, 506 and 629 cm^{-1} can be identified as the E_g, F_{2g} (two modes) and A_{1g} first-order Raman active modes typical of ZFO.[44] Also the broad weak feature at around 1120 cm^{-1} can be assigned to ZFO,[45] despite its similarity with the Raman signature of magnetite (Fe_3O_4).[46,47] More importantly, the absence of the characteristic intense signal of α-Fe_2O_3 at 1320 cm^{-1} and of the broad band above 1400 cm^{-1} typical of γ-Fe_2O_3 confirms the absence of undesired hematite[48,49] or maghemite,[50] respectively.

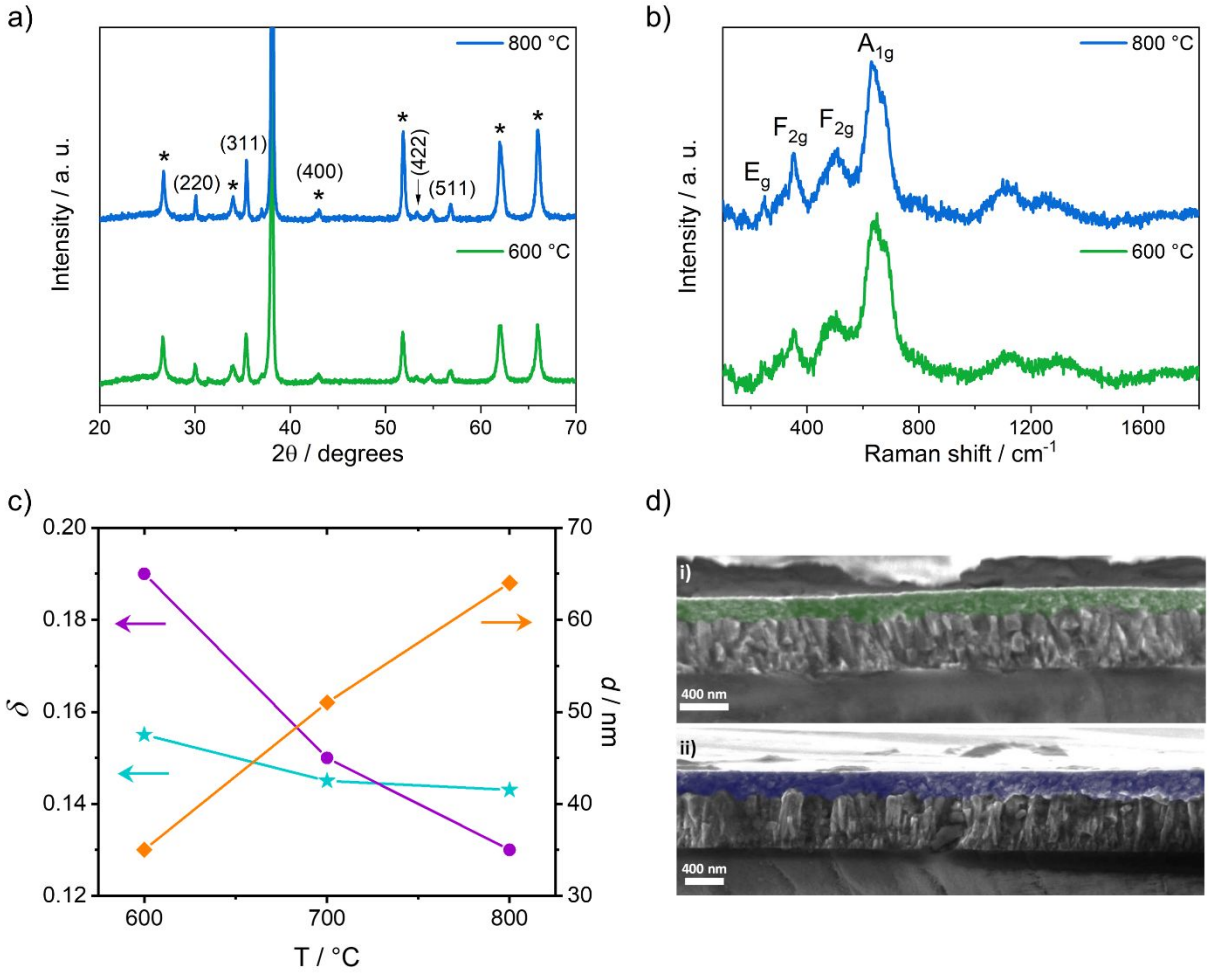

Figure 1. (a) XRD patterns and (b) Raman spectra of representative ZFO films annealed at 600 °C and 800 °C; (c) trends in the spinel inversion degree δ for our planar ZFO films (purple circles) and for ZFO NR electrodes (cyan stars, reproduced from ref. 38) and in the estimated crystalline domain size d (orange diamonds) *vs.* the synthesis temperature; (d) cross section SEM images of the (i) *ca.* 220 nm and (ii) *ca.* 240 nm-thick films annealed at 600 °C (Mag = 25.62 K X) and 800 °C (Mag = 20.55 K X), respectively, employed for the α evaluation reported in Section 2.3.

Despite the apparent phase purity of our ZFO thin films, additional investigation of the crystallinity of the material prepared via our sol-gel route is valuable considering the crystal structure of $ZnFe_2O_4$, which can exist in normal and inverted configurations. Indeed, typically ZFO possesses an almost normal spinel crystal structure composed of a cubic closed-packed array of oxygen atoms with the Zn^{2+} and Fe^{3+} ions located at the tetrahedral and octahedral sites, respectively.[51] However, cation inversion can occur and the degree of inversion (δ), defined as the fraction of tetrahedral sites occupied by Fe^{3+} ions, is known to mainly affect the magnetic behaviour of spinel ferrites.[52,53]

According to Thota *et al.*,[39] the A_{1g} mode in Raman spectra (**Figure 1b**), which is representative of the symmetric stretching of tetrahedral units, may split into two separate peaks associated with the lattice vibrations in the tetrahedral positions of both Zn and Fe cations, in the presence of an inversion degree. Based on this, the only slight A_{1g} mode split detectable in the peaks at 648 and 680 cm^{-1} of both Raman spectra shown in **Figure 1b** may indicate a partial inversion degree in the synthesized films.

Note that δ was suggested to influence the PEC properties of ZFO samples with NR morphology even more than their crystallinity degree.[40] Accordingly, we next estimated the crystalline domain size and cation inversion as a function of the synthesis temperature via the Rietveld refinement of PXRD patterns (**Figure S2**) of ZFO powders prepared at 600 °C, 700 °C and 800 °C using a procedure similar to that employed to prepare our thin films. In **Figure 1c** we display the values of δ, and the crystalline domain size (estimated by the integral breadth), d, as a function of the synthesis temperature. The same inverse behaviour for δ and d is observed with increasing preparation temperature as for ZFO NR samples,[40] although with a significantly different relative variation degree of these two parameters. In particular, while d monotonically increases by *ca.* 50% when rising the preparation temperature from 600 °C to 800 °C, the cation disorder δ exhibits only a minor decrease, from 0.15 to 0.14, for the same synthesis temperature increase. A much higher decrease in cation disorder was found for the ZFO NR electrodes within the same temperature range, with δ dropping from *ca.* 0.20 to 0.13 (data reproduced in Figure 1c for comparison).[40] Moreover, the maximum δ value of 0.15 achieved in the case of the planar ZFO films is far below $\delta = 1$ expected for a totally inverted spinel structure, suggesting that our as-prepared planar ZFO films primarily exhibit the normal spinel phase. The difference in the trend of δ between the planar films and the NR films is likely due to the synthesis method, where for the NR morphology an intermediate goethite phase of FeOOH is used. On the other hand, with respect to the crystal domain size, the remarkable increase (*ca.* 50%) of d from 35 to 65 nm (**Figure 1c**) in the planar films, which is comparable with the *ca.*

70% increase observed in NR films,[40] indicates a significant enhancement in crystallinity upon rising the synthesis temperature, in agreement with other reports.[45]

The morphology of the ZFO films was next examined by electron microscopy. **Figure 1d** shows representative cross-section SEM images of films prepared starting from the 7.5 M in [Fe^{3+}] and 3.75 M in [Zn^{2+}] ZFO precursor solution and prepared at either 600 °C (**Figure 1d i**) or 800 °C (**Figure 1d ii**). A planar film geometry is observed with dense and compact layers composed of interconnected nanoparticles with comparable thickness in the 220–240 nm range, regardless of the synthesis temperature.

3.2 Photoelectrochemical performance

Typical current density *vs.* applied potential (*J-V*) curves were collected under standard water oxidation conditions (intermittent 1-Sun illumination, 1.0 M NaOH electrolyte), to investigate how the different parameters (*i.e.* the synthesis temperature, film thickness, and hydrogen treatment) affect the PEC performance. **Figure 2** summarizes the *J-V* results in a plot of the photocurrent density at 1.5 V *vs.* RHE as a function of the film thickness, recorded under both back (substrate-side) and front (electrolyte-side) illumination of either the pristine or the hydrogen-treated electrodes prepared at 600 or 800 °C. The reported values are averaged over 5 electrodes prepared in the same conditions (see **Figure S3**). The relatively small error bars underline the reproducibility of the adopted synthesis method and post-synthesis hydrogen treatment. The results shown in **Figure 2** for hydrogen-treated electrodes refer to a 1 h-long exposure to H_2 flux, as prolonging the reductive treatment up to 4 h did not produce any further PEC performance improvement, as shown in **Figure S4**. This suggests that the film composition equilibrium in terms of oxygen vacancies was already reached after 1 h-long reductive treatment.

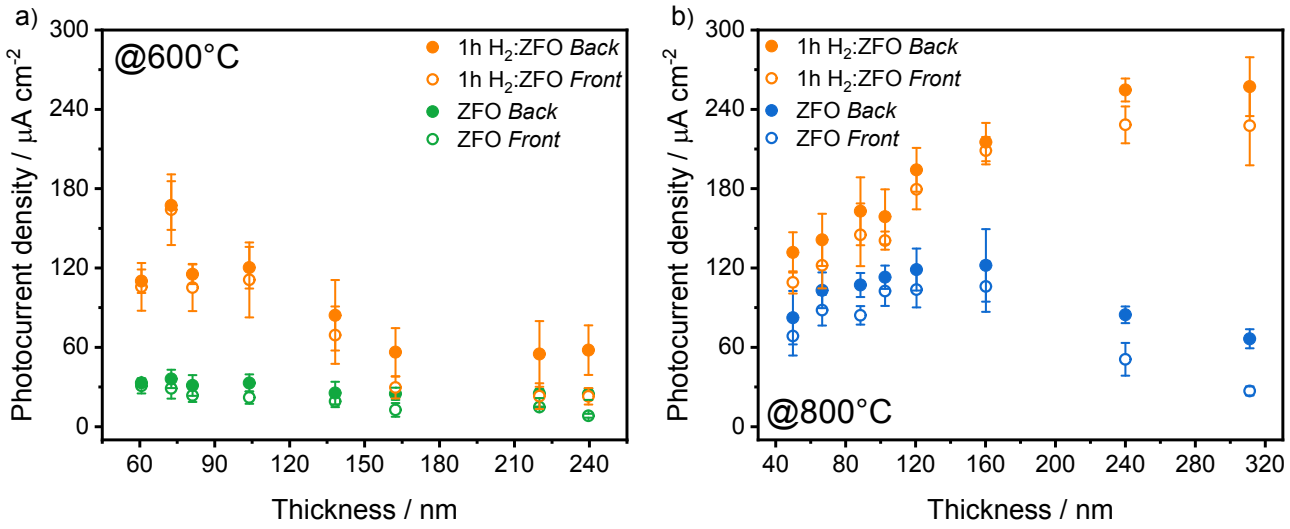

Figure 2. Photocurrent density (*J*) values as a function of the film thickness recorded with (a) the 600 °C and (b) the 800 °C electrodes at 1.5 V *vs.* RHE, before (pristine, green and blue) and after 1 h-long H_2-treatment (orange). Reported *J* values are the average of linear sweep voltammetry measurements with different samples in 1.0 M NaOH solution under either back (full circles) or front side (void circles) irradiation.

A clearly different behaviour for the pristine and the H_2 treated electrodes depending on the synthesis temperature is revealed by the data in **Figure 2**. Focusing on pristine films, the electrodes prepared at 600 °C (**Figure 2a**, green markers) exhibit a low photocurrent (below 40 μA cm^{-2}) that is insensitive to film thickness. In view of the relatively low crystallinity of the pristine 600 °C films, as evidenced by the *d* values reported in **Figure 1c**, the poor performance is consistent with a limitation in photogenerated charge transport. In contrast, the higher crystallinity of the films prepared at 800 °C, and likely the diffusion of Sn^{4+} dopant from the FTO substrate[23], correlated to a higher activity of the pristine electrodes, with a bell-shaped trend of the photocurrent *vs.* the film thickness and a maximum of 130 μA cm^{-2} around 160 nm, followed by a decrease for thicker films (**Figure 2b**, blue markers). This behaviour is also consistent with a limitation in photogenerated charge transport in films with thickness greater than 160 nm and the lower performance of the thicker films from the front side illumination points to a limitation in the transport of the majority charge carriers.

After H_2-treatment, the overall PEC performance increased but to a very different extent depending on the film thickness and preparation temperature. Indeed, while among the hydrogen-treated less crystalline (600 °C) electrodes the maximum photocurrent was recorded at a low thickness

(70 nm), followed by a drop with increasing thickness (**Figure 2a**, orange markers), the reduction treatment applied to more crystalline films (800 °C) induced a progressive enhancement in PEC performance with increasing film thickness, up to a plateau at 240 nm (**Figure 2b**, orange markers). The behaviour here observed for electrodes of thickness smaller than 100 nm is consistent with our previous results on ZFO planar films with similar thickness (under 100 nm),[41] while a much larger increase in performance after hydrogenation can be observed for the more crystalline (800 °C) electrodes series at the highest film thicknesses. For both preparation temperatures a maximum 4-fold enhancement in photocurrent was obtained upon H_2-treatment, though largely different absolute photocurrent values were attained in the two cases. In fact, the maximum photocurrent density of the hydrogen-treated electrodes initially prepared at 600 °C was only 160 μA cm^{-2}, while the combination of a higher (800 °C) preparation temperature and a subsequent hydrogen treatment boosted the photocurrent density of thicker photoactive layers up to 260 μA cm^{-2}, the maximum value attained in the present study.

To highlight the effects of H_2-treatment on films with different thickness prepared at the two temperatures, we focused on the results obtained with the 70 nm- and the 240 nm-thick films of each series. **Figure 3** shows the complete *J-V* curves recorded with these electrodes, either before or after H_2-treatment, under back side illumination. These curves exhibit typical n-type photoanode behaviour, with a photocurrent onset around 0.8 V *vs.* RHE, in agreement with previous studies,[11,23,39–41] and sharp transient photocurrent spikes at low bias, indicative of relatively high interfacial recombination, until a higher bias is attained where charges are extracted without accumulation and recombination. The transient spikes are more pronounced in the case of less crystalline films prepared at 600 °C. Moreover, the hydrogen treatment has a different impact on the shape of the *J-V* curve, depending on the thickness and preparation temperature. In fact, a higher saturation photocurrent (at high bias, *e.g.* 1.5 V *vs.* RHE) and an improved photocurrent onset in the low applied potential region were achieved upon H_2-treatment of optimal ZFO_70@600 (**Figure 3a)** and ZFO_240@800 (**Figure 3d**). In contrast, only a minor performance increase was attained upon

hydrogen treatment of ZFO_240@600 (**Figure 3b**), while treatment of ZFO_70@800 induced a performance decrease with a later photocurrent onset potential and a lower fill factor, compared to the pristine film (**Figure 3c**).

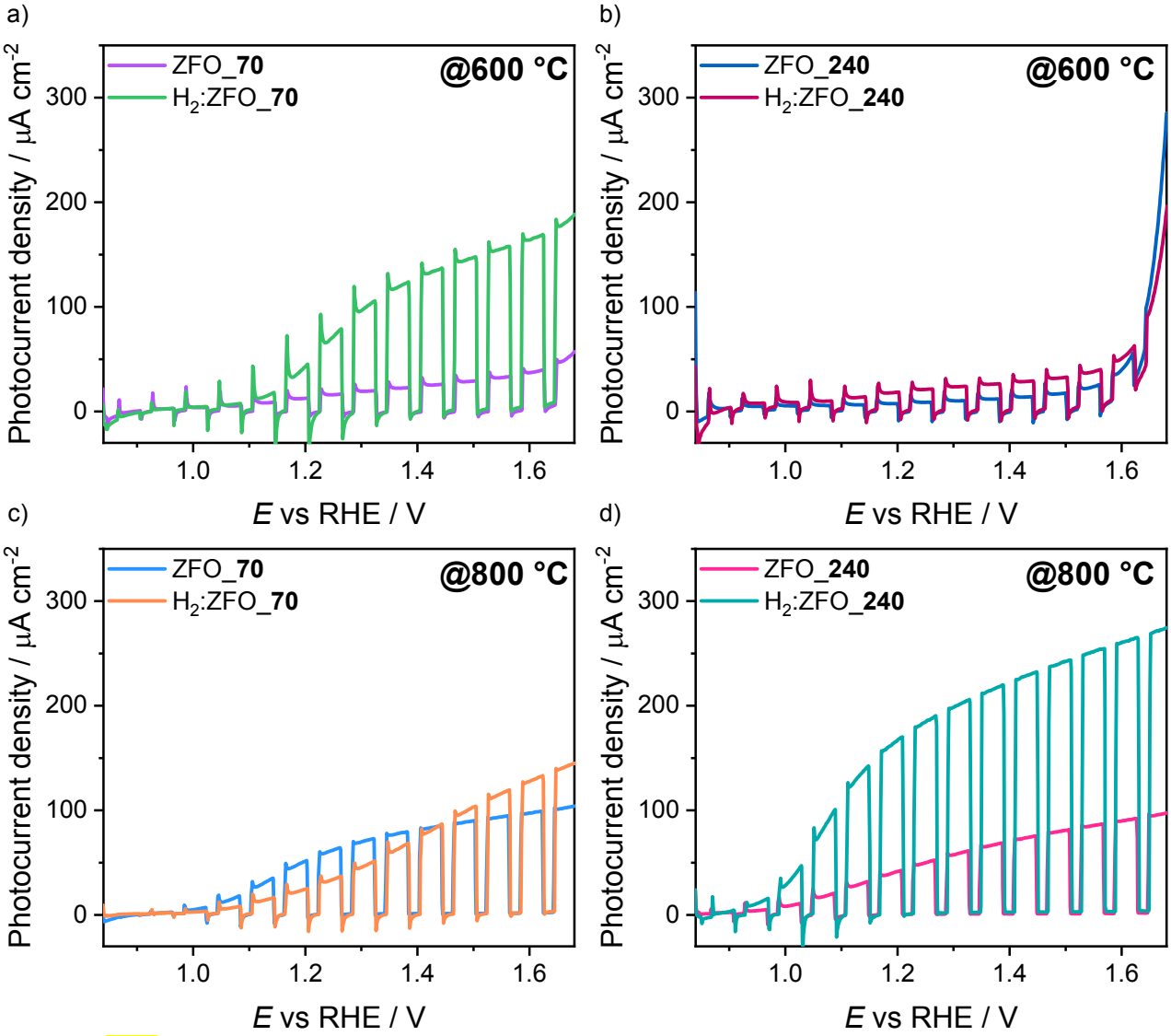

Figure 3. LSV plots recorded in 1.0 M NaOH electrolyte solution under back side irradiation, with 70 nm- and 240 nm-thick films prepared at (a,b) 600 °C or (c,d) 800 °C, before and after 1 h-long H_2 treatment.

The photocurrent onset potential of water oxidation is very sensitive to the presence of defects that cause surface recombination, due to the narrow width of the space charge layer in the low applied potential region.[54] Indeed, an increased surface defect concentration can cause Fermi-level pinning which may be reflected by a delay of the photocurrent onset potential with respect to the flatband potential.[23,45] Thus, the delayed photocurrent onset potential of the H_2-treated ZFO_70@800 electrode compared to the pristine one may indicate that the hydrogen treatment has a detrimental

effect on the surface properties of this sample, *e.g.* by introducing oxygen vacancies acting as surface trap states.[27,33,55]

To shed light onto the origin of the different impact of the H_2 treatment onto the PEC performance of ZFO films, depending on both their thickness and synthesis temperature, the bulk charge separation and the surface charge injection contributions to the overall photocurrent were decoupled by using sacrificial conditions[56] (Na_2SO_3 hole scavenger, see **Figure S5**) to extract the photogenerated charge separation efficiency (η_{sep}) and the minority charge carrier injection efficiency (η_{inj}). Indeed, the water oxidation photocurrent density can be expressed as $J_{H2O} = J_{abs}\,\eta_{sep}\,\eta_{inj}$, where J_{abs} is the theoretical maximum photocurrent density considering the light absorbed by each film, calculated from the integration of the product between the standard AM 1.5 G solar spectrum and the absorption spectrum of the electrode, over the proper absorption wavelengths range. Analogously, by assuming a 100% charge injection efficiency for Na_2SO_3 oxidation ($\eta_{inj} = 1$),[56] the photocurrent of sulfite oxidation (J_{Na2SO3}) is such that $J_{Na2SO3} = J_{abs}\,\eta_{sep}$, from which η_{sep} can be simply obtained by dividing the photocurrent measured in the presence of the Na_2SO_3 hole scavenger by J_{abs}. From the combination of the two photocurrent expressions (in the presence and absence of hole scavenger) one can finally calculate η_{inj}, which is equal to the ratio between J_{H2O} and J_{Na2SO3}.

The calculated efficiencies for the thinnest and thickest films of the two investigated electrode series are reported in **Figure 4** as a function of the applied potential. In all cases, η_{sep} values are much lower than η_{inj} values, indicating that the photocurrent response of our planar ZFO photoanodes is ultimately governed by a severe bulk recombination, possibly due to either a very low mobility and diffusion length of the carriers (*e.g.* due to polaron formation) or a high density of bulk defects. The bulk charge separation efficiency of the pristine samples typically increases gradually with increasing bias, due to the progressive widening of the depletion region adjacent to the electrode/electrolyte interface,[56] though it remains below 4% in all cases. These low η_{sep} values are in line with those reported for nanostructured ZFO[23,26–28,57] and decrease when moving from the thinner (**Figure 4a,c**) to the thicker films (**Figure 4b,d**) within each electrodes series, likely due to the increased probability

of bulk recombination with increasing thickness. A slight increase in charge separation can be observed when moving from samples annealed at 600 °C to those at 800 °C when considering the same thickness (Figure 4). This evidences the minor impact of the synthesis temperature on η_{sep}. Moreover, the H_2 treatment induces a conspicuous improvement of the charge separation efficiency compared to that of the pristine films, up to a maximum 3-fold enhancement at 1.5 V *vs.* RHE (**Figure 4c**); only for the poorly crystalline thicker film, exhibiting an intrinsically low η_{sep}, this remains low also after H_2-treatment (**Figure 4b**). This can be reasonably explained by the larger amount of charge carriers that should be produced by a thicker film and that, in case of poor crystallinity, may lead to an increased charge accumulation at the SCLJ,[23,26,27,33,55,58] which can be responsible for the lack of improvement in η_{sep} besides η_{inj} after H_2-treatment.

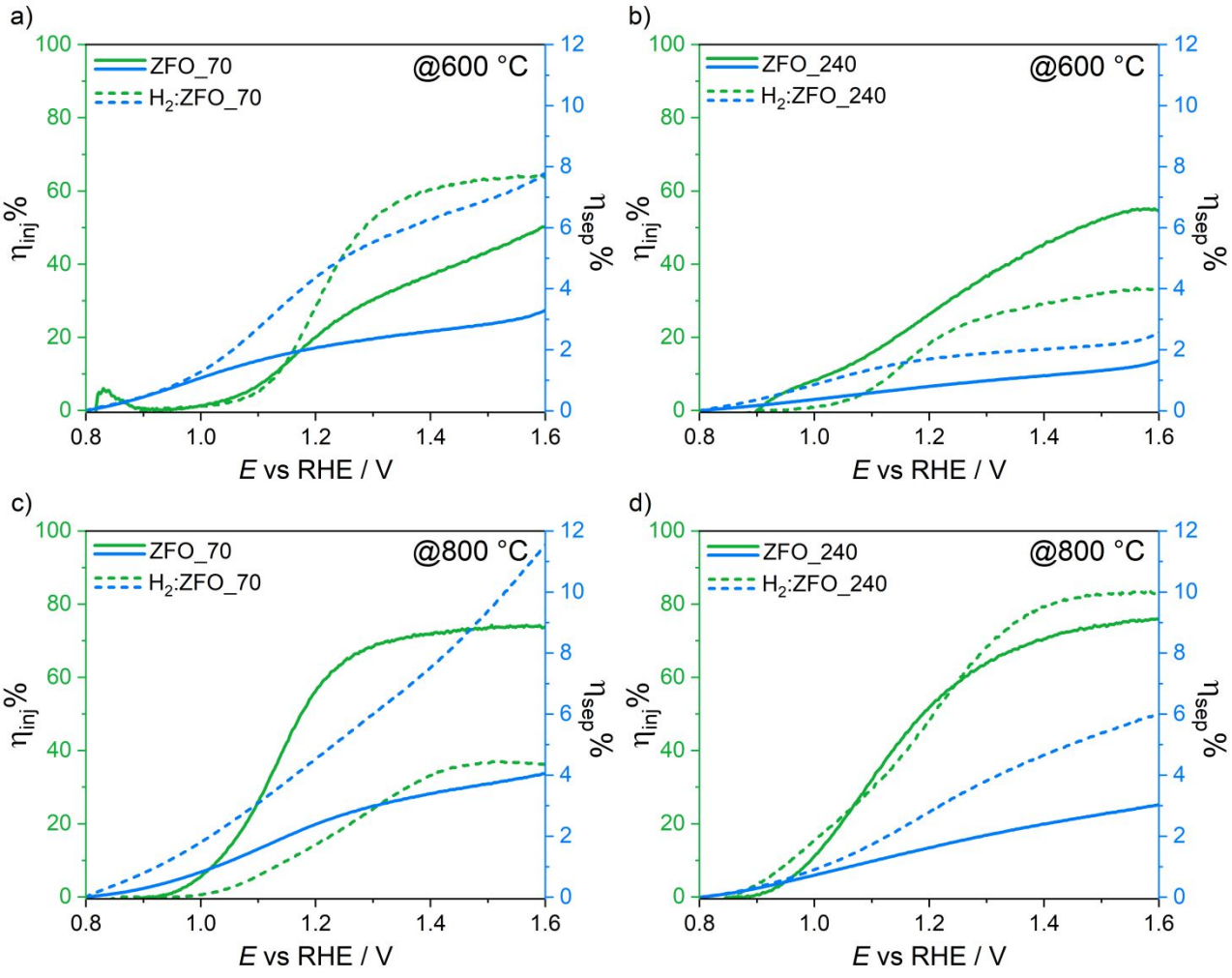

Figure 4. Charge injection (η_{inj}, green) and charge separation (η_{sep}, blue) efficiencies of the 70 nm- and 240 nm-thick films prepared at either (a,b) 600 °C or (c,d) 800 °C, before (continuous lines) and after 1 h-long H_2-treatment (dashed lines).

In contrast to its minor effects in the bulk charge separation efficiencies, the synthesis temperature has a great impact on the charge transfer efficiencies at the SCLJ interface. In fact, focusing on pristine samples, the more crystalline films prepared at 800 °C (**Figure 4c,d**) exhibit a η_{inj} close to 80% already at 1.4 V *vs.* RHE, which is double than that shown by the less crystalline electrodes annealed at 600 °C (**Figure 4a,b**). Moreover, for the electrodes annealed at 800 °C, this plateau value is achieved with a steeper η_{inj} increase at the photocurrent onset potential compared to the electrodes prepared at 600 °C, which indicates an efficient mitigation of surface recombination with increasing band bending.[23,56] A similar η_{inj} behaviour, independent of the film thickness, was observed with ZFO electrodes with NR morphology[26,40] annealed at similar temperatures.

On the other hand, the impact of the H_2 treatment on the surface injection strictly depends on both the film thickness and the preparation temperature, inducing a slight improvement for best performing ZFO_70@600 and ZFO_240@800 in the high potential region. This indicates that the hydrogen treatment has a little impact on the surface injection properties of planar ZFO samples.

3.3 Intensity Modulated Photocurrent Spectroscopy

PEC analyses conducted in the presence of sacrificial agents might not be representative of true water oxidation conditions since either the space charge properties (*e.g.* band-bending) or the charge accumulation at the photoanode surface can be influenced by the nature of the redox species involved in the electrochemical reaction at the film/electrolyte interface.[59] Therefore, caution should be taken in evaluating η_{sep} and η_{inj} for water oxidation, which is affected by a large surface kinetics bottleneck, from measurements carried out under sacrificial conditions, *i.e.* under the assumption that no charge accumulation occurs at the SCLJ. In fact, especially in the presence of a significant charge accumulation at the SCLJ under sluggish oxidation conditions, η_{sep} and η_{inj} values estimated from sacrificial measurements may considerably differ from the real ones. For this reason and aiming at validating the results obtained from PEC measurements in the presence of Na_2SO_3, η_{sep} and η_{inj} were also evaluated *in operando* by means of IMPS measurements, conducted under water photo-oxidation conditions in 1.0 M NaOH electrolyte. IMPS has indeed proved to be a powerful frequency domain

tool to unequivocally decouple the bulk and surface contributions of photoanodes by their respective time constants.[60,61]

The IMPS response for the same eight investigated electrodes shown in **Figure 4** is shown in **Figure 5** as Nyquist plots of the complex photocurrent at 1.5 V *vs.* RHE, which can be directly compared to the *J* at the same bias reported in **Figure 2**.

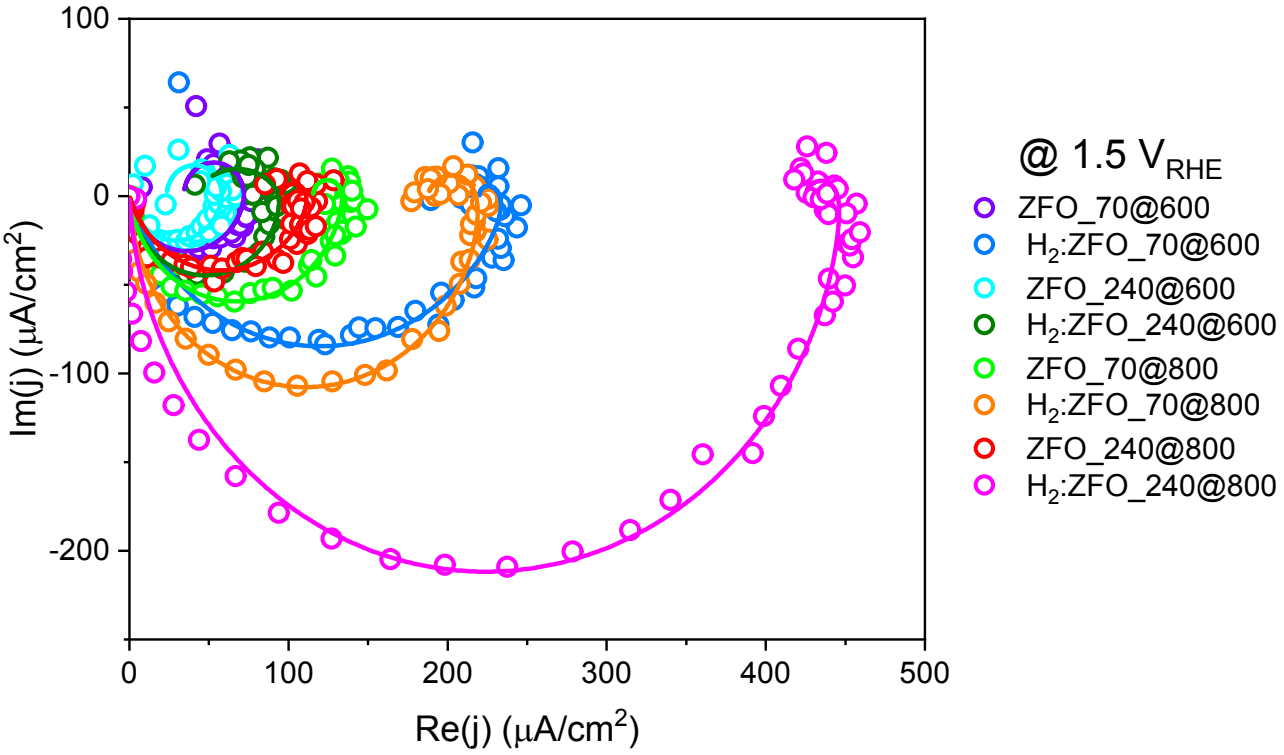

Figure 5. IMPS analyses at 1.5 V *vs.* RHE for the 70 nm- and 240 nm-thick films prepared at either 600 °C or 800 °C. The represented raw data (circles) and fitted model (lines) were obtained upon normalization to the electron current recorded at the IMPS setup.

All Nyquist plots are composed of two semicircles: the negative semicircle located in the lower quadrant and representative of the higher frequency process (shorter time constant), corresponding to charge transport in the bulk, and the positive semicircle located in the upper quadrant and associated with surface recombination occurring at lower frequencies (longer time constant).[62] Specifically, the amplitudes of the negative and positive semicircles are directly indicative of the flux of holes arriving to the SCLJ that are available for water oxidation (J_h) and the flux of holes that are lost by surface recombination (J_r), respectively. Therefore, the significantly smaller surface recombination semicircle in comparison with the bulk transport semicircle observable

in all reported cases (in **Figure 5**) indicates that a large steady state photocurrent is available for water oxidation at the surface of our planar ZFO photoanodes, in analogy with other metal oxide photoanodes.[63,64] All details about the IMPS model fitting and the extracted parameters, *i.e.* two photocurrent amplitudes (J_h and J_r) and the corresponding time constants for bulk hole current (τ_h) and surface recombination (τ_r), are reported in the Supporting Info, **Figure S6**. On the basis of model employed for the IMPS analysis,[62] an accurate estimate of the η_{sep} and η_{inj} parameters *in operando* can be pursued by simply calculating them as $\eta_{sep} = J_h/J_{abs}$ (where J_{abs} is the maximum photocurrent expected for each ZFO film based on its absorbance spectrum) and $\eta_{inj} = (J_h - J_r)/J_h$. **Figure 6** shows the comparison of these quantities extracted at 1.5 V *vs.* RHE for all investigated electrodes.

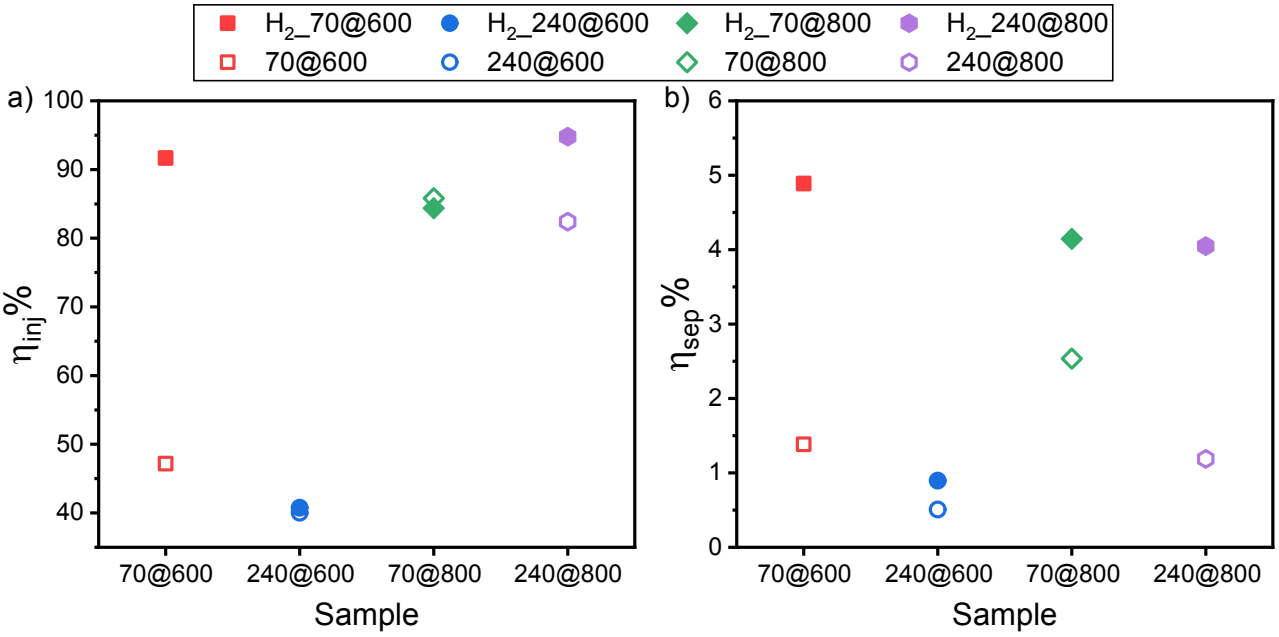

Figure 6. (a) Charge injection (η_{inj}) and (b) charge separation (η_{sep}) efficiencies calculated from IMPS data at 1.5 V *vs.* RHE, for the 70 nm- and 240 nm-thick films prepared at either 600 °C or 800 °C, before and after 1 h-long H_2-treatment.

The results of IMPS measurements conducted *in operando* confirm the trends of η_{sep} and η_{inj} obtained from PEC measurements in the presence of a sacrificial agent. The huge discrepancy between the surface injection and the bulk separation efficiencies is even more marked in this case, with maximum values of 95% (η_{inj}) and 5% (η_{sep}), respectively, and accounts for bulk charge separation as main performance limiting issue. The already-assessed effects of both synthesis

temperature and H_2 treatment on the two decoupled contributions, in relation to the film thickness, are confirmed. While the charge injection efficiency doubles from *ca.* 40% to *ca.* 80% in pristine samples prepared at higher temperature, regardless of the film thickness, H_2-treatment does not markedly influence the charge transfer efficiency at the photoanode surface, except for one case (**Figure 6a**). In fact, beyond the highest increase in η_{inj} detected for the hydrogen-treated thinner film prepared at 600 °C compared to its pristine form, a slight improvement of the surface injection properties occurs after H_2-treatment also for the thicker electrode prepared at 800 °C, likely induced by the passivation of surface states affecting the performance of the pristine samples.

On the other hand, the calculated charge separation efficiencies (**Figure 6b**) appear very sensitive to both the film thickness and the reductive treatment. In agreement with the results obtained under sacrificial conditions, the η_{sep} values of the pristine films decrease with increasing film thickness, for both synthesis temperatures. Consequently, the modest improvement in charge separation induced by the higher synthesis temperature can be appreciated only for the thinner film of the series.

In this picture, H_2 treatment plays a crucial role by inducing a remarkable improvement of the bulk charge separation in almost all cases, up to a maximum 4-fold enhancement observed with best performing ZFO_70@600 and ZFO_240@800. Moreover, as a result of the higher H_2-treatment efficiency observed with the thicker film within the 800 °C series, its η_{sep} attains the same value as the reduced form of the thinner film, despite the two electrodes exhibit significantly different efficiencies prior to H_2-treatment. A different extent of η_{sep} increase upon H_2-treatment can be observed within the 800 °C electrodes series, with the highest η_{sep} relative increase attained with the thickest ZFO_240@800 electrode. This can be explained by considering the different strength of the electric field resulting from polarizing the two samples (especially at a potential as high as 1.5 V *vs.* RHE), depending on their thickness and doping density, which in turn influence the width of the space charge region. In fact, a stronger electric field, responsible for the better charge separation observed among the pristine electrodes, is expected in the thinner with respect to the thicker electrode, since a

similar voltage drop occurs over a smaller distance. On the other hand, after H_2-treatment any relevant further gain in electric field under polarization of the thinner ZFO_70@800 film is prevented by the narrowing of the depletion region caused by the increase in donor density, according to PEIS analyses (see Section 3.4).

Therefore, H_2 treatment performed on the more crystalline films prepared at 800 °C enhances their bulk charge separation up to a maximum value regardless of the film thickness, beyond which the performance of the electrodes is ultimately governed by their photon absorption capability. A different behaviour is observed for the less crystalline samples calcined at 600 °C, with an increase in η_{sep} upon H_2 treatment for the thinner film of the series only.

3.4 Electrochemical Impedance Spectroscopy

Electrochemical impedance spectroscopy experiments were conducted under standard water oxidation conditions (1-Sun illumination, 1.0 M NaOH electrolyte) in back-side configuration, on the ZFO_70@600 and ZFO_160@800 films, in both pristine and hydrogen-treated forms. The PEIS data were fitted to a modified Randles circuit, consisting of a series resistance R_S, a bulk capacitance C_{bulk} such that $C_{bulk}^{-1} = C_{SC}^{-1} + C_H^{-1}$, where C_{SC} is the space charge layer capacitance and C_H the Helmholtz capacitance, a parallel resistance of hole trapping to surface states R_{trap}, a surface state capacitance C_{SS} and a charge transfer resistance from surface states to oxidize water $R_{ct,SS}$. The Mott-Schottky (M-S) plots for the investigated electrodes, constructed with the values of C_{SC} plotted as a function of the applied potential, are shown in **Figure S7**.

The fitting parameters, *i.e.* the donor density values N_D and the flatband potential E_{FB} calculated from the slope and extrapolated from the abscissa-intercept of each M-S plot, respectively, are reported in **Table 2**, together with the space charge layer width (W) at 1.5 V *vs.* RHE, calculated according to the following equation:[65]

$$W = \sqrt{\frac{2\varepsilon\varepsilon_0}{qN_D}|E - E_{FB}|} \quad \#(2)$$

where ε is the dielectric constant of ZFO, ε_0 is vacuum permittivity and q is elementary charge. Data relative to both pristine ZFO_70@600 and hydrogen-treated H_2 ZFO_70@600 are omitted in Table 2 since the M-S model could not be applied to these films (illogical values were obtained for the M-S plot reported in **Figure S7a**).

Table 2. Flatband potential, E_{FB}, and donor density, N_D, values calculated from M-S analyses and space charge width, W, calculated from equation (2).

Sample	E_{FB} / V_{RHE}	N_D / cm^{-3}	W @ 1.5 V_{RHE} / nm
ZFO_160@800	0.80	$1.7 \cdot 10^{18}$	70
H_2 ZFO_160@800	0.80	$2.7 \cdot 10^{19}$	17

The extrapolated flatband potential is in good accordance with the photocurrent onset potentials of the *J-V* plots reported in **Figure 3**. The one order of magnitude N_D increase attained upon H_2-treatment of the more crystalline ZFO_160@800 film compared to its pristine form clearly suggests that an increase in donor density is provided by H_2-treatment, demonstrating its n-type character, able to enhance the electron conductivity of the films.

From the measured donor density values, a reduction of the space charge layer width from 70 to 17 nm can be detected upon H_2-treatment of the ZFO_160@800 sample, according to **Eq. 2**. Although the estimation of W for the pristine ZFO_70@600 film is not possible, it is reasonable to guess that a decrease in W might have occurred also upon H_2-treatment of the less crystalline sample.

4. Discussion

Merging the results obtained through PEC measurements in the presence of the sacrificial agent with those of IMPS analyses conducted *in operando*, allows to interpret the photocurrent trends at 1.5 V *vs.* RHE reported in **Figure 2** in light of the obtained η_{sep} and η_{inj} trends.

The poor crystallinity induced by the lower preparation temperature clearly results in the presence of a large amount of both bulk and surface defects responsible for the low bulk charge separation and surface charge injection efficiencies of the less crystalline films annealed at 600 °C, in turn leading to their almost flat trend in photocurrent as a function of the film thickness (**Figure**

2a). Preparing the ZFO at higher temperature (800 °C) mainly improves the charge injection efficiency at the ZFO photoanode/electrolyte interface for any film thickness, likely through the deactivation of surface trapping states at this interface, as a consequence of the gain in film crystallinity according to PXRD analysis (**Figure S2**).[54]

While the same η_{inj} behaviour was observed for ZFO NR electrodes,[40] the charge transport in planar ZFO films should be primarily governed by the crystallinity of the material[66] rather than by the cation disorder, at difference with respect to ZFO NR as supported by the trends in d and δ shown in **Figure 1c**. A minor enhancement in charge separation with rising the synthesis temperature can be observed at low thickness only (**Figure 6b**), resulting in the photocurrent drop observed among the pristine electrodes prepared at 800 °C after the optimal 160 nm thickness (**Figure 2b**). This behaviour can be reasonably ascribed to the progressive increase in bulk resistance to charge transport and/or to the decreased effect of the built-in electric field generated in the space charge region with increasing thickness.

On the other hand, hydrogen treatment exerts its main impact on the charge separation efficiency, which underwent up to a 4-fold enhancement with best performing ZFO_240@800 after H_2-treatment (**Figure 6b**). This reflects the well-established doping effect of H_2-treatment, known to enhance the performance of metal oxide photoanodes through the introduction of oxygen vacancies acting as electron donors.[23,27,55,67] In this way, charge separation across the bulk of the film could benefit from the enhanced majority carrier density, since that will increase the built-in electric field across the space charge region[68] and enhance the film conductivity, both contributing to an improved electron transport.[27,55,67]

Hydrogen treatment improves charge separation at the various film thicknesses to a largely different extent depending on the initial ZFO synthesis temperature, being much more beneficial to the more crystalline films prepared at 800 °C (**Figure 2b**). Among them, a higher H_2-treatment efficiency in terms of a larger improvement in η_{sep} is attained when moving towards the thicker film of the series (**Figure 6b**), where the optimization of the charge separation in the thicker photoactive

layer combined with its superior absorption capability allows for the actual exploitation of a larger amount of photogenerated couples.

The reductive treatment applied on the poorly crystalline films induces a significant η_{sep} increase in the thinner electrode only, while a negligible improvement is observed with the hydrogen-treated thicker film compared to its pristine form (**Figure 6b**). This behaviour can be ascribed to the very poor crystallinity imparted by the lower preparation temperature, which hampers charge transport over thick films.

Minor effects, strongly dependent on both film thickness and synthesis temperature, were produced by H_2-treatment on the charge injection properties at the photoanode surface, as ascertained through both PEC measurements in the presence of the sacrificial agent and IMPS analyses.

The combined use of the higher 800 °C preparation temperature for effective surface charge injection and of hydrogen doping for an improved bulk charge transport is essential to maximize the performance of our planar ZFO films.

5. Conclusions

The interplay between synthesis temperature, film thickness and reductive H_2-treatment treatment onto the PEC performance of optically transparent planar ZFO photoanodes for water oxidation has been here elucidated. IMPS measurements performed *in operando* allowed to identify the role of the preparation temperature and hydrogen treatment separately onto the surface charge injection and bulk charge separation processes, as a function of the film thickness. The superior crystallinity of the electrodes prepared at higher temperature increases the performance of our ZFO pristine films and ensures an enhanced bulk charge separation upon H_2-treatment, though remaining below *ca.* 10% due to the intrinsic poor electronic conductivity of zinc ferrite material associated with a strong bulk recombination. The complementary roles played by the here-optimized synthesis parameters should be exploited to construct efficient ZFO photoanodes to be implemented in PEC tandem cells where planar geometry is an important requirement for high optical film transparency.

Acknowledgements

The authors thank Dr. P.A. Schouwink (EPFL) for support with XRD measurements. This research was partially funded by the MIUR PRIN 20173397R7 MULTI-e project, and by the Swiss National Science Foundation (SNSF) under the grant PZENP2_166871.

References

1 S. J. Davis, N. S. Lewis, M. Shaner, S. Aggarwal, D. Arent, I. L. Azevedo, S. M. Benson, T. Bradley, J. Brouwer, Y. M. Chiang, C. T. M. Clack, A. Cohen, S. Doig, J. Edmonds, P. Fennell, C. B. Field, B. Hannegan, B. M. Hodge, M. I. Hoffert, E. Ingersoll, P. Jaramillo, K. S. Lackner, K. J. Mach, M. Mastrandrea, J. Ogden, P. F. Peterson, D. L. Sanchez, D. Sperling, J. Stagner, J. E. Trancik, C. J. Yang and K. Caldeira, *Science*, 2018, **360** (6396), No. eaas9793.

2 D. G. Nocera, *Acc. Chem. Res.*, 2017, **50**, 616–619.

3 I. Roger, M. A. Shipman and M. D. Symes, *Nat. Rev. Chem.*, 2017, **1**, 0003/1–13.

4 J. H. Kim, D. Hansora, P. Sharma, J. W. Jang and J. S. Lee, *Chem. Soc. Rev.*, 2019, **48**, 1908–1971.

5 J. Qi, W. Zhang and R. Cao, *Adv. Energy Mater.*, 2018, **8**, 1–16.

6 Y. Dai, J. Yu, C. Cheng, P. Tan and M. Ni, *J. Mater. Chem. A*, 2020, **8**, 6984–7002.

7 S. D. Tilley, *Adv. Energy Mater.*, 2019, **9**, 1–13.

8 M. S. Prévot and K. Sivula, *J. Phys. Chem. C*, 2013, **117**, 17879–17893.

9 J. H. Kim, H. Kaneko, T. Minegishi, J. Kubota, K. Domen and J. S. Lee, *ChemSusChem*, 2016, **9**, 61–66.

10 C. Jiang, S. J. A. Moniz, A. Wang, T. Zhang and J. Tang, *Chem. Soc. Rev.*, 2017, **46**, 4645–4660.

11 C. R. Lhermitte, A. Polo, L. Yao, F. A. Boudoire, N. Guijarro and K. Sivula, *ChemSusChem*, 2020, **13**, 3645–3653.

12 T. Higashi, H. Nishiyama, Y. Suzuki, Y. Sasaki, T. Hisatomi, M. Katayama, T. Minegishi, K. Seki, T. Yamada and K. Domen, *Angew. Chemie - Int. Ed.*, 2019, **58**, 2300–2304.

13 J. H. Kim, J.-W. Jang, Y. H. Jo, F. F. Abdi, Y. H. Lee, R. van de Krol and J. S. Lee, *Nat. Commun.*, 2016, **7**, 13380/1–9.

14 K. Sivula, *J. Phys. Chem. Lett.*, 2013, **4**, 1624–1633.

15 K. Sivula and R. van de Krol, *Nat. Rev. Mater.*, 2016, **1**, 15010/1–16.

16 C. R. Lhermitte and K. Sivula, *ACS Catal.*, 2019, **9**, 2007–2017.

17 Y. Yang, S. Niu, D. Han, T. Liu, G. Wang and Y. Li, *Adv. Energy Mater.*, 2017, **7**, 1700555/1–26.

18 D. K. Lee, D. Lee, M. A. Lumley and K.-S. Choi, *Chem. Soc. Rev.*, 2019, **48**, 2126–2157.

19 F. F. Abdi and S. P. Berglund, *J. Phys. D. Appl. Phys.*, 2017, **50**, 193002/1–22.

20 F. E. Osterloh, *Chem. Soc. Rev.*, 2013, **42**, 2294–2320.

21 R. Dillert, D. H. Taffa, M. Wark, T. Bredow and D. W. Bahnemann, *APL Mater.*, 2015, **3**, 104001/1–15.

22 L. G. J. de Haart, *J. Electrochem. Soc.*, 1985, **132**, 2933–2938.

23 N. Guijarro, P. Bornoz, M. Prévot, X. Yu, X. Zhu, M. Johnson, X. Jeanbourquin, F. Le Formal and K. Sivula, *Sustain. Energy Fuels*, 2018, **2**, 103–117.

24 J. H. Kim, H. E. Kim, J. H. Kim and J. S. Lee, *J. Mater. Chem. A*, 2020, **8**, 9447–9482.

25 A. G. Hufnagel, K. Peters, A. Müller, C. Scheu, D. Fattakhova-Rohlfing and T. Bein, *Adv. Funct. Mater.*, 2016, **26**, 4435–4443.

26 J. H. Kim, J. H. Kim, J.-W. Jang, J. Y. Kim, S. H. Choi, G. Magesh, J. Lee and J. S. Lee, *Adv. Energy Mater.*, 2015, **5**, 1401933/1–9.

27 J. H. Kim, Y. J. Jang, J. H. Kim, J. W. Jang, S. H. Choi and J. S. Lee, *Nanoscale*, 2015, **7**, 19144–19151.

28 J. H. Kim, Y. J. Jang, S. H. Choi, B. J. Lee, J. H. Kim, Y. Bin Park, C.-M. Nam, H. G. Kim and J. S. Lee, *J. Mater. Chem. A*, 2018, **6**, 12693–12700.

29 Y. Guo, N. Zhang, X. Wang, Q. Qian, S. Zhang, Z. Li and Z. Zou, *J. Mater. Chem. A*, 2017, **5**, 7571–7577.

30 J. H. Kim, Y. J. Jang, S. H. Choi, B. J. Lee, M. H. Lee and J. S. Lee, *ACS Sustain. Chem. Eng.*, 2019, **7**, 944–949.

31 W. Gao, R. Peng, Y. Yang, X. Zhao, C. Cui, X. Su, W. Qin, Y. Dai, Y. Ma, H. Liu and Y. Sang, *ACS Energy Lett.*, 2021, 2129–2137.

32 J. H. Kim, J. H. Kim, J. H. Kim, Y. K. Kim and J. S. Lee, *Sol. RRL*, 2020, **4**, 1900328–1900338.

33 Y. Liu, M. Xia, L. Yao, M. Mensi, D. Ren, M. Grätzel, K. Sivula and N. Guijarro, *Adv. Funct. Mater.*, 2021, **31**, 2010081–2010088.

34 S. Kim, M. A. Mahadik, W. S. Chae, J. Ryu, S. H. Choi and J. S. Jang, *Appl. Surf. Sci.*, 2020, **513**, 145528–145544.

35 T. H. Jeon, G. hee Moon, H. Park and W. Choi, *Nano Energy*, 2017, **39**, 211–218.

36 J. Y. Kim, G. Magesh, D. H. Youn, J. W. Jang, J. Kubota, K. Domen and J. S. Lee, *Sci. Rep.*, 2013, **3**, 1–8.

37 A. A. Tahir and K. G. U. Wijayantha, *J. Photochem. Photobiol. A Chem.*, 2010, **216**, 119–125.

38 J. Wang, Y. Wang, X. Xv, Y. Chen, X. Yang, J. Zhou, S. Li, F. Cao and G. Qin, *Dalt. Trans.*, 2019, **48**, 11934–11940.

39 K. Kirchberg, S. Wang, L. Wang and R. Marschall, *ChemPhysChem*, 2018, **19**, 2313–2320.

40 X. Zhu, N. Guijarro, Y. Liu, P. Schouwink, R. A. Wells, F. Le Formal, S. Sun, C. Gao and K. Sivula, *Adv. Mater.*, 2018, **30**, 1801612/1–6.

41 A. Polo, C. R. Lhermitte, M. V. Dozzi, E. Selli and K. Sivula, *Surfaces*, 2020, **3**, 93–104.

42 W. Q. Hong, *J. Phys. D. Appl. Phys.*, 1989, **22**, 1384–1385.

43 S. Murcia-López, C. Fàbrega, D. Monllor-Satoca, M. D. Hernández-Alonso, G. Penelas-Pérez, A. Morata, J. R. Morante and T. Andreu, *ACS Appl. Mater. Interfaces*, 2016, **8**, 4076–4085.

44 Z. Wang, D. Schiferl, Y. Zhao and H. S. C. O'Neill, *J. Phys. Chem. Solids*, 2003, **64**, 2517–2523.

45 D. Peeters, D. H. Taffa, M. M. Kerrigan, A. Ney, N. Jöns, D. Rogalla, S. Cwik, H. W. Becker, M. Grafen, A. Ostendorf, C. H. Winter, S. Chakraborty, M. Wark and A. Devi, *ACS Sustain. Chem. Eng.*, 2017, **5**, 2917–2926.

46 K. Murugappan, D. S. Silvester, D. Chaudhary and D. W. M. Arrigan, *ChemElectroChem*, 2014, **1**, 1211–1218.

47 O. N. Shebanova and P. Lazor, *J. Solid State Chem.*, 2003, **174**, 424–430.

48 W. S. Bourée, M. S. Prévot, X. A. Jeanbourquin, N. Guijarro, M. Johnson, F. Le Formal and K. Sivula, *Adv. Mater.*, 2016, **28**, 9308–9312.

49 D. L. A. De Faria, S. Venâncio Silva and M. T. De Oliveira, *J. Raman Spectrosc.*, 1997, **28**, 873–878.

50 N. S. Chaudhari, S. S. Warule, S. Muduli, B. B. Kale, S. Jouen, B. Lefez, B. Hannoyer and S. B. Ogale, *Dalt. Trans.*, 2011, **40**, 8003–8011.

51 F. Bræstrup, B. C. Hauback and K. K. Hansen, *J. Solid State Chem.*, 2008, **181**, 2364–2369.

52 S. Bid and S. K. Pradhan, *Mater. Chem. Phys.*, 2003, **82**, 27–37.

53 C. N. Chinnasamy, A. Narayanasamy, N. Ponpandian, K. Chattopadhyay, H. Guérault and J. M. Greneche, *J. Phys. Condens. Matter*, 2000, **12**, 7795–7805.

54 O. Zandi and T. W. Hamann, *J. Phys. Chem. Lett.*, 2014, **5**, 1522–1526.

55 X. Zhao, J. Feng, S. Chen, Y. Huang, T. C. Sum and Z. Chen, *Phys. Chem. Chem. Phys.*, 2017, **19**, 1074–1082.

56 H. Dotan, K. Sivula, M. Grätzel, A. Rothschild and S. C. Warren, *Energy Environ. Sci.*, 2011, **4**, 958–964.

57 Y. Lan, Z. Liu, Z. Guo, M. Ruan and Y. Xin, *J. Colloid Interface Sci.*, 2019, **552**, 111–121.

58 N. Sato, *Electrochemistry at Metal and Semiconductor Electrodes*, Elsevier, Elsevier, edn. 1998.

59 D. Klotz, D. A. Grave and A. Rothschild, *Phys. Chem. Chem. Phys.*, 2017, **19**, 20383–20392.

60 E. A. Ponomarev and L. M. Peter, *J. Electroanal. Chem.*, 1995, **396**, 219–226.

61 D. Klotz, D. S. Ellis, H. Dotan and A. Rothschild, *Phys. Chem. Chem. Phys.*, 2016, **18**, 23438–23457.

62 F. Boudoire, Y. Liu, F. Le Formal, N. Guijarro, C. R. Lhermitte and K. Sivula, *J. Phys. Chem. C*, 2021, **125**, 10883–10890.

63 Y. Liu, F. Le Formal, F. Boudoire, L. Yao, K. Sivula and N. Guijarro, *J. Mater. Chem. A*, 2019, **7**, 1669–1677.

64 Y. Liu, F. Le Formal, F. Boudoire and N. Guijarro, *ACS Appl. Energy Mater.*, 2019, **2**, 6825–6833.

65 M. X. Tan, P. E. Laibinis, S. T. Nguyen, J. M. Kesselman, C. E. Stanton and N. S. Lewis, ed. John Wiley & Sons, 2007, pp. 21–144.

66 S. C. Warren, K. Voïtchovsky, H. Dotan, C. M. Leroy, M. Cornuz, F. Stellacci, C. Hébert, A. Rothschild and M. Grätzel, *Nat. Mater.*, 2013, **12**, 842–849.

67 M. Rioult, D. Stanescu, E. Fonda, A. Barbier and H. Magnan, *J. Phys. Chem. C*, 2016, **120**, 7482–7490.

68 M. S. Prévot, N. Guijarro and K. Sivula, *ChemSusChem*, 2015, **8**, 1359–1367.